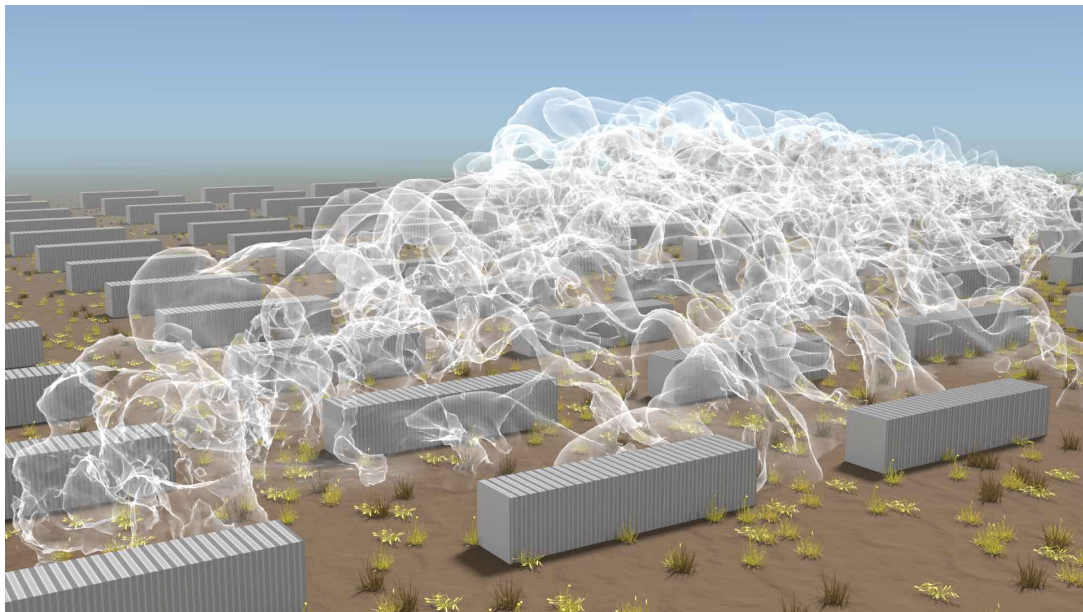


CERFACS
2021 Technical Report TR-CMGC-21-72

Large-eddy simulation multi-model
comparison of the MUST trial 2681829

M.C. Rochoux, E. Lumet, L. Thouron, G. Rea, F. Auguste, T. Jaravel & O. Vermorel

October 2021



Foreword

This work was carried out at CERFACS during the time period 2016-2021, and results provided us confidence in the ability of large-eddy simulations (LES) obtained with AVBP and Meso-NH to represent microscale environmental flows in complex geometry such as urban areas. A comparison of different LES was carried out for one MUST/*Mock Urban Setting Test* trial, with the objective of providing a first estimate of structural model uncertainties. This comparison was done without considering inflow turbulence injection. We will revisit this aspect in the near-future to provide a full and complete study on structural model uncertainty estimation for microscale atmospheric flows.

The financial support provided by the FCS-STAE foundation is greatly appreciated. This work was granted access to the HPC resources from GENCI-TGCC/CINES (Grants 2017–A0010110079 and 2019–A0062A10822). The authors acknowledge Bertrand Carissimo (EDF R&D), Eric Pardyjak (University of Utah) and Daniel Cariolle (Météo-France) for helpful discussions and for providing data on both environmental CFD and MUST datasets. They also acknowledge Benjamin Farcy, Vincent Moureau and Ghislain Lartigue (CORIA) for support on YALES2, Juan Escobar (LA) for support on Meso-NH, Rémy Fransen (CERFACS) for support on visualisation as well as the Computer Support Group at CERFACS.

1 Introduction

Quantifying air pollution exposure has been identified as a valuable research objective with direct applications in air quality prediction and in health and environmental impact assessment. Air pollutants (trace gases such as sulfur dioxide, nitric oxides, ammonia and aerosols) are released into the atmosphere from multiple sources associated with natural hazards (e.g. wildfires, [Langmann et al., 2009]) and anthropogenic daily emissions [Crippa et al., 2016]. Air pollutants can also be released from industrial plant accidents [Armand et al., 2014, Auguste et al., 2020, Farchi et al., 2016]. They can degrade air quality and have significant short- and long-term health and environmental impacts [EEA, 2017]. They are dispersed over a wide range of length and time scales and may deposit on land/ocean surfaces by scavenging (e.g. acid rain) or dry deposit processes. Tracking the pollutant concentrations is therefore a multi-scale problem ranging from the near field (within a few metres away from the source) to the far field (at scales ranging from a few hundred metres up to the global scale).

Simulating the near field is particularly challenging. Pollutant concentrations can locally vary by orders of magnitude in time and space due to the complex turbulent flow dynamics induced by surface heterogeneity, in particular in urban areas where separation and recirculation zones are induced by the presence of buildings of different height and geometry [Fernando et al., 2001, Klein et al., 2007, Franke et al., 2011, Tominaga and Stathopoulos, 2013, Hertwig et al., 2019]. A variety of dispersion models exists in the literature, with different levels of physical modelling resulting from a balance between accuracy and computational cost [Holmes and Morawska, 2006, Leelóssy et al., 2014]. At the operational level, the smoke plume formed by the air pollutants is

usually parameterized using cost-effective Gaussian dispersion models with empirical parameters and strong assumptions, for instance on meteorological conditions [Carruthers et al., 1994, Cimorelli et al., 2005, Perry et al., 2005, Soulhac et al., 2011, Soulhac et al., 2012]. Several complex physical processes such as atmospheric stratification, buoyancy, chemistry or deposition can be included. However, the near-field interactions between the smoke plume and the complex flow dynamics are simplified and are not fully representative of what is occurring in reality. An alternative to Gaussian dispersion models is Lagrangian models simulating short-range trajectories of air pollutants [Challa et al., 2008]. However, these models may have a too coarse resolution to simulate the wind field for a highly heterogeneous surface.

Relevant insight into the atmospheric flow patterns, the near-surface turbulence and their impacts on the pollutant dispersion in the near field has been obtained via micro-scale Computational Fluid Dynamics (CFD) [Baklanov, 2000, Di Sabatino et al., 2007, de Sampaio et al., 2008, Antonioni et al., 2012, Tominaga and Stathopoulos, 2013, Working group “GT 3D dispersion”, 2015, Hayati et al., 2017, Toparlak et al., 2017]. This framework explicitly solves for the pollutant concentration transport equation based on the velocity field obtained from the Navier-Stokes equations. Detailed information can be obtained on the flow dynamics and pollutant concentration at the early stage of the smoke plume. Reynolds-Averaged Navier-Stokes (RANS) approaches have contributed to the emergence of micro-scale CFD. With these approaches, flow turbulence properties are fully modelled, using for instance a classical $k-\epsilon$ model or a second-moment closure model [Meroney et al., 1999, Milliez and Carissimo, 2007, Koutsourakis et al., 2012]. However, capturing the unsteady flow and tracer concentration fluctuations may be important to locate peak concentrations and predict short-term exposure. That is why despite their computational cost, Large-Eddy Simulations (LES) are becoming popular to represent time and space variability of turbulent atmospheric flows [Patnaik et al., 2007, Dejoan et al., 2010, Gousseau et al., 2011, Harms et al., 2011, Moonen et al., 2012, Aumond et al., 2013, Bergot et al., 2015, Vervecken et al., 2015a, García-Sánchez et al., 2018, Merlier et al., 2018]: with LES the large turbulent scales characterizing the flow are explicitly solved and only the smaller scales are modelled using a subgrid turbulence model, providing access to local flow and concentration statistics in the dispersion problem. [García-Sánchez et al., 2018] have shown the improved accuracy of LES over the RANS simulations, except where the solution is highly sensitive to the inflow boundary conditions. LES is now used to formulate parametrization for operational air quality models grylls2019.

Validation is an important process to ensure quality and fidelity of such CFD approaches for real cases [Meyers, 2008, Blocken and Gualtieri, 2012]. Comparing numerical simulations and experimental measurements in terms of mean and turbulent fluctuations provides a way to evaluate the computer model strengths, limitations and its capability to represent reality. Only a limited number of full-scale experiments are available for validation due to their complexity and cost, for instance the “Joint Urban 2003 field experiment” in Oklahoma City that is fully representative of urban geometric complexity [Allwine et al., 2004]. More datasets combining field and laboratory scale experiments are available [Hanna et al., 2002], for instance the CEDVAL wind tunnel datasets [Hamburg University, 2002] or the MUST (Mock Urban Setting Test) field experiment corresponding to an idealized urban area [Yee and Biltoft, 2004]. MUST is an attractive test case

for a deep assessment of the LES reliability and quality for air pollution micrometeorology: i) the urban canopy has a reduced size and is simplified to a regular array of shipping containers, making the LES affordable while keeping real meteorological conditions; and ii) observations of wind, turbulence and tracer concentration are available at different locations throughout the field.

The MUST dataset has been used in several studies, mainly to evaluate RANS simulations and carry out comparative analysis for different inflow boundary conditions [Hanna et al., 2004, Milliez and Carissimo, 2007, Donnelly et al., 2009, Kumar et al., 2015]. All these studies are based on mean statistical metrics and found relatively good agreement with the experimental measurements. To go beyond steady simulations and give access to flow and concentration temporal fluctuations, some studies have also evaluated the quality of LES [Camelli et al., 2005, König, 2014] and provided a detailed comparison to that of RANS [Dejoan et al., 2010, Santiago et al., 2010]. While the mean flow patterns were correctly retrieved by RANS simulations, LES were found to bring additional information on the tracer concentration fluctuations, which are of paramount importance to assess emergency planning and response as well as air quality impact on health and environment.

In this paper, the objective is to go further into the evaluation of LES quality by comparing different LES models for a given MUST near-neutral case. Simulations are performed with three LES solvers, AVBP [Schönfeld and Rudgyard, 1999, Gourdain et al., 2009], Meso-NH [Lafore et al., 1998, Lac et al., 2018] including an Immersed Boundary Method (IBM) [Auguste et al., 2019], and YALES2 [Moureau et al., 2011, Malandain et al., 2013], resulting in different numerical set-ups (in terms of model equations, computational grids, numerical schemes, physical assumptions). A pool of eight LES models is then formed by sampling several sources of uncertainty in the LES codes, i.e. by changing some of the numerical or physical components for each code (e.g. computational mesh, subgrid turbulence, advection schemes). A detailed model-to-model comparison over the resulting multi-model ensemble is proposed to i) validate LES against MUST observations, and ii) estimate the influence of modelling and numerical choices in the LES response and accuracy.

The present study contributes to quantifying through a multi-model ensemble, some of the model structural uncertainties (i.e. uncertainties inherent to the choice of the code and the underlying model assumptions) in micro-scale LES and thereby assessing the quality of the LES models for environmental flows. This is inline with current research efforts to improve the representation of atmospheric boundary layer processes using LES [Couvreur et al., 2020] and more generally to characterize model bias in Earth System modelling [Williamson et al., 2015, Qian et al., 2018]. Questions related to aleatory uncertainties, i.e. uncertainties inherent to the natural variability of the physical system, for instance to the meso-scale meteorological variability [Yamada and Koike, 2011, Temel and van Beeck, 2016, García-Sánchez and Górlé, 2018, Defforge et al., 2019], are not addressed here. Estimating the model structural uncertainties can be seen as a first step towards estimating the total uncertainties in micro-scale LES, which would be useful to inform future model development efforts and design reduction strategy to improve operational models [Vervecken et al., 2015b, Grylls et al., 2019].

The outline of this paper is as follows. The MUST trial is first presented in Sect. 2. The main features of AVBP, Meso-NH and YALES2 are described in Sect. 3 with numerical details of the

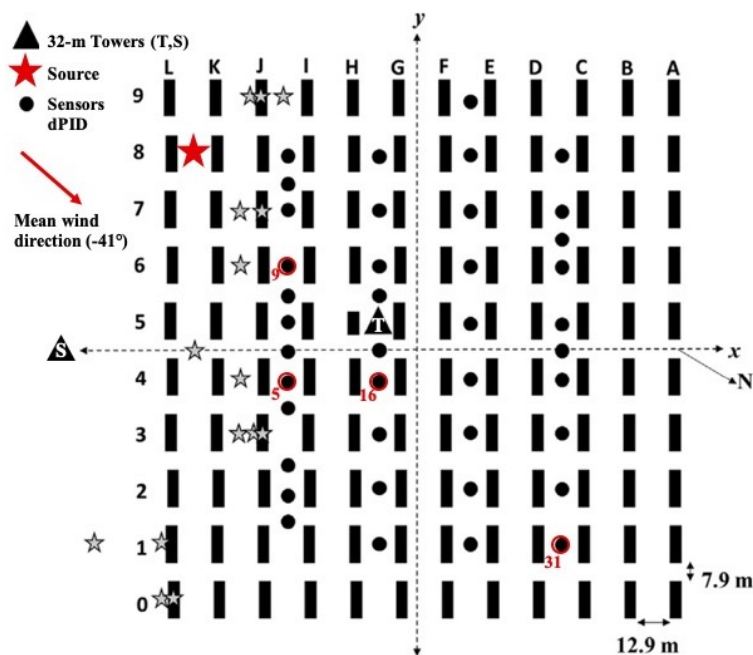


Figure 1: Schematic representation of the MUST configuration (horizontal cut) adapted from [Kumar et al., 2015]. The array of containers (black rectangles) is described in terms of columns (from A to L) and in terms of lines (from 0 to 9). The location of the experimental sensors is indicated (black circles); sensors 5, 9, 16 and 31 used in Sect. 5 are indicated in red. The tracer source location (red star) and the mean wind direction (red arrow) corresponding to the trial 2681829 are also indicated.

MUST simulations in Sect. 4. Results are finally provided and discussed in Sect. 5.

2 The MUST (Mock Urban Setting Test) Experiment

MUST is a field-scale experiment performed in September 2001 in Utah, USA, and sponsored by the Defense Threat Reduction Agency (DTRA) to provide extensive measurements in the short-to-medium range of a plume within a urban-like canopy in support of the development and validation of urban dispersion models [Biltoft, 2001, Yee and Biltoft, 2004]. This canopy is mimicked by an array of 120 regularly-spaced shipping containers made of 10 lines (numbered from 0 to 9) and 12 columns (named from A to L) such that container A0 is located in the north-east corner of the array and container L0 is located in the south-east corner of the array (Fig. 1). The container dimensions are 12.2 m long, 2.42 m wide and 2.54 m high. The distances between two columns and two lines are 12.9 m and 7.9 m, respectively. The terrain is flat and homogeneous with a mix of sparse greasewood and sagebrush that is from 0.4 to 0.75 m high. Some small geometrical irregularities were present in the way the containers were arranged. We consider here a regular case as for instance in [Milliez and Carissimo, 2007]. The impact of the geometrical irregularities on the flow field was studied in [Dejoan et al., 2010], but they were not found to have a significant impact on the spatial average flow properties.

Table 1: Main characteristics of the MUST trial 2681829 [Yee and Biltoft, 2004]: α_4 and u_4 are respectively the mean wind direction and the mean horizontal wind speed at the 4-m level of tower S; L_o is the Obukhov length at the 4-m level of tower T (location of towers S and T is given in Fig. 1); Q is the tracer release rate; and z_s is the source height.

Trial	Local start time UTC	α_4 ($^\circ$)	u_4 (m s^{-1})	L_o (m)	Q (L min^{-1})	z_s (m)
2681829	2001/09/25 1830	-41	7.93	28,000	225	1.8

A non reactive gas (propylene C_3H_6), referred to as “tracer”, was released at different locations during 15 minutes, for different atmospheric conditions (several wind directions, wind speeds and atmosphere states) across the field.

40 concentration sensors (black circles in Fig. 1) were available to measure tracer concentration (with a detection threshold of 0.04 ppm – parts per million) at height $z = 1.6$ m within the canopy. Two 32-m towers (black triangles in Fig. 1) were also deployed, the central tower T (located in the canopy between columns H and G) and the upstream tower S (located 30 m upstream the first column – column L – of containers), which provide wind components measurements at $z = 4, 8$ and 16 m. From these observations, 21 trials were selected by [Yee and Biltoft, 2004] for their high quality (i.e. tracer detection on the tower T and for three of the four sampling columns) and for their near-stationary state (the large-scale forcing can be considered stationary during the experiment).

In this work, we simulate one of the 21 trials referred to as 2681829, whose main characteristics extracted from the data of yee2004 at towers S and T are summarized in Table 1. This case is a configuration with near-neutral atmospheric conditions (i.e. afternoon transition from unstable to stable conditions), characterized by a high value of the Obukhov length L_o ($L_o > 2,500$ m at the 4-m level of tower T), no latent and sensible heat fluxes, and a weak influence of buoyancy. This case is thus particularly relevant to study the container impact on the incident flow and in particular the plume deflection from the inlet wind direction within the container array. The mean wind speed u_4 and the mean wind direction α_4 at $z = 4$ m at the upstream tower S are respectively 7.93 m s^{-1} and -41 (this angle is defined with respect to the x -axis of the container array indicated in Fig. 1, the north direction corresponding to an angle of -30). These conditions correspond to a moderate wind mainly blowing from the south-southwest direction. The gas was released at $z_s = 1.8$ m after column L and on line 8 of containers (red star symbol in Fig. 1) with a continuous flow rate Q of 225 L min^{-1} . The same case 2681829 was studied by [König, 2014] in LES mode, and in RANS mode as part of a set of MUST trials, for instance in [Milliez and Carissimo, 2007] and [Kumar et al., 2015].

3 Large-Eddy Simulation (LES) Solvers

In this work, simulations have been performed with three different massively parallel LES codes, AVBP, Meso-NH and YALES2, and for various numerical set-ups to test the sensitivity of the results

to the choice of model components and numerical parameters. These codes were adopted since they are research references in their communities for LES, AVBP and YALES2 in fluid mechanics community, and Meso-NH in atmospheric boundary layer community.

Meso-NH¹ [Lafore et al., 1998, Lac et al., 2018], developed by both Météo-France and Laboratoire d'Aérodynamique, is a non-hydrostatic anelastic (i.e. incompressible) structured code. Meso-NH is used for various atmospheric flows, mainly at meso-scale (few kilometres to less than thousand kilometres) but also at higher resolution [Filippi et al., 2018, Sabatier et al., 2020a, Sabatier et al., 2020b]. A development version of Meso-NH including an IBM model is used here to simulate atmospheric flows at micro-scale [Auguste et al., 2019, Auguste et al., 2020]. YALES2² is an unstructured code developed at CORIA [Moureau et al., 2011, Malandain et al., 2013] solving for the low-Mach Navier-Stokes equations with constant or variable density flow. YALES2 is mainly used for reactive and turbulent flows in complex geometry [Locci et al., 2018]. AVBP³ [Schönfeld and Rudgyard, 1999, Gourdain et al., 2009] is a compressible and unstructured code developed by CERFACS. AVBP is widely used to resolve reactive unsteady flows in complex industrial geometry such as gas turbine or rocket engine; it is also particularly relevant to predict pollutant formation and near-field dispersion in the atmosphere [Poubeau et al., 2016, Paoli et al., 2019].

A general description (physical assumptions, numerical schemes and models, computational grids, initial and boundary conditions) of these codes is provided in this section. Each code is used (for the so-called “reference” run) in its best-known configuration, i.e. with its a priori best models and options in terms of numerics, boundary conditions or closure models for instance. Table 2 summarizes the main settings used in these reference simulations. It is worth mentioning that none of these three codes has been used here in its classic application framework. The MUST test case is the first near-real case simulated using the IBM in Meso-NH. AVBP and YALES2 are not usually applied to environmental fluid flows in open areas. The present study can therefore be considered as a validation test case for the three codes. Their best-known settings may not hold for the MUST test case. So sensitivity tests are carried out to evaluate their strengths and limitations.

3.1 Governing Equations

For the three codes, the LES formalism implies to solve the filtered Navier-Stokes equations. Denoting by ρ the air density and u_j ($j = 1, \dots, 3$) the velocity components, the general form of the equations for these filtered quantities can be written as

$$\frac{\partial \rho}{\partial t} + \frac{\partial}{\partial x_i}(\rho u_i) = 0, \quad (1)$$

$$\frac{\partial}{\partial t}(\rho u_j) + \frac{\partial}{\partial x_i}(\rho u_i u_j) = -\frac{\partial p}{\partial x_j} + \frac{\partial(\tau_{ij} + \tau_{ij}^t)}{\partial x_i} + \rho' g_j, \quad (2)$$

¹Meso-NH documentation, see <http://mesonh.aero.obs-mip.fr/mesonh52/>

²YALES2 documentation, see <https://www.coria-cfd.fr/index.php/YALES2>

³AVBP documentation, see <http://www.cerfacs.fr/avbp7x/>

where p is the pressure, τ_{ij} is the viscous stress tensor, τ_{ij}^t is the subgrid turbulent stress tensor, and g_j is the gravity component.

The tracer scalar satisfies

$$\frac{\partial}{\partial t}(\rho r) + \frac{\partial}{\partial x_i}(\rho u_i r) = -\frac{\partial}{\partial x_i}(j_r + j_r^T) + \rho S_r, \quad (3)$$

where ρr is the tracer mass concentration (in mass of tracer per unit volume of gas), j_r is the tracer diffusion flux, j_r^T the subgrid tracer diffusion flux, and S_r is the source term corresponding to the local release (without chemical reactions since the tracer is considered as passive).

For the present test case, a near-neutral atmospheric state is observed, meaning that there is no buoyant effect in practice ($\rho' = 0$). Different assumptions on the air density ρ are made for the three codes. In YALES2, a Boussinesq approximation is used, i.e. $\rho = \rho_0$, where ρ_0 is constant in space and time. Meso-NH relies on the anelastic assumption and thereby assumes that ρ only varies vertically so that $\rho = \langle \rho(z) \rangle$, where $\langle \rho(z) \rangle$ represents the mean horizontal density that is uniform over the whole vertical level z . Hence, for Meso-NH and YALES2, the continuity equation simplifies to $\partial \rho u_i / \partial x_i = 0$. In AVBP, the fully compressible equations are solved, which include an equation for the total energy E (i.e. the sum of sensible and kinetic energies) satisfying

$$\frac{\partial}{\partial t}(\rho E) + \frac{\partial}{\partial x_i}(\rho u_i E) = -\frac{\partial}{\partial x_i}(j_T + j_T^t) + \frac{\partial}{\partial x_j}(\sigma_{ij} u_i) + \rho' g_j u_j, \quad (4)$$

where j_T is the thermal molecular diffusion flux, j_T^t is the subgrid thermal flux, and σ_{ij} is the tensor including viscous and pressure effects so that $\sigma_{ij} = \tau_{ij} + \tau_{ij}^t - p \delta_{ij}$. The system is closed with the state equation $p = \rho(R/W)T$, where R is the perfect gas constant, T is the air temperature and W is the air molecular weight.

Since AVBP is a fully compressible LES solver, the time-step is highly constrained by the CFL condition for acoustic wave propagation. Since correctly capturing the acoustic waves is not relevant in the context of atmospheric boundary layer simulation (very low Mach number, Ma), an artificial compressibility approach also known as pressure gradient scaling [Ramshaw et al., 1986, Wang and Trouvé, 2004] is adopted for AVBP. The propagation speed of the acoustic waves (c) is artificially decreased by rescaling the pressure p and the temperature T by a factor α^2 , leading to artificial temperature and pressure (denoted with * superscript):

$$T^* = \alpha^2 T, \quad p^* = \alpha^2 p. \quad (5)$$

With this transformation, the resulting acoustic wave propagation speed (c^*) is artificially reduced by a factor α as shown by the following equation:

$$c^* = \sqrt{\gamma r T^*} = \sqrt{\gamma r \alpha^2 T} = \alpha c, \quad (6)$$

where γ is the heat capacity ratio, which significantly reduces the constraint on the AVBP model time-step. It can be shown that the hydrodynamic problem remains unchanged [Ramshaw et al., 1986], provided the resulting artificial Mach number $Ma^* = Ma/\alpha$ remains small. In the present study,

Table 2: Reference numerical configurations for Meso-NH, YALES2 and AVBP used to simulate the MUST trial 2681829. In bold are indicated the components that are changed in the sensitivity tests.

Codes	Meso-NH	YALES2	AVBP
<u>Code settings</u>			
Equations	Incompressible, anelastic	Low-Mach	Artificial compressibility
Container condition	IBM ^a	Body fitted	Body fitted
Advection scheme	WENO5^b (5th order in space, 4th order in time)	TFV4A ^d (4th order in space and time)	TTGC^f (3rd order in space and time)
Subgrid turbulence	TKE 1.5 ^c	WALE^e	WALE^e
<u>MUST case</u>			
Time step	0.012 s	< 0.02 s	6.5×10^{-4} s
Grid type	Structured	Unstructured	Unstructured
Grid size	135 million cells	71 million cells	71 million cells
Number of cores	1,920	1,600	1,440
Total CPU time ^g	40,000 h	21,000 h	21,600 h

^a [Auguste et al., 2019]

^b [Lunet et al., 2017]

^c [Cuxart et al., 2000]

^d [Kraushaar, 2011]

^e [Nicoud and Ducros, 1999]

^f [Colin and Rudgyard, 2000]

^g The total CPU time corresponds to the cost associated with a MUST run on the CINES/OC-CIGEN supercomputer (part of the French network provided by GENCI).

α is set to 0.22 to guarantee that $Ma^* < 0.1$ in the whole simulation domain. Several numerical tests (not shown here but presented in thouron2020, thouron2020) have demonstrated that the AVBP simulation obtained with artificial compressibility provides very similar results as the standard AVBP simulation but with a reduced computational cost (by a factor of about 5 for the MUST test case).

3.2 Numerics and Models

Meso-NH uses a fourth-order explicit Runge-Kutta scheme for time integration associated with either a fourth-order CENtered scheme (CEN4) or a fifth-order Weight Essential Non Oscillatory scheme (WENO5) [Liu et al., 1994] for wind advection combined with the Piecewise Parabolic Method (PPM) [Colella and Woodward, 1984] for meteorological variables and tracer advection. For the reference Meso-NH simulation, WENO5 is used as it features good accuracy and stability with no need of artificial diffusion and as it reduces computational cost compared to CEN4 [Lunet et al., 2017]. Comparison between CEN4 and WENO5 simulations is performed in Sect. 5.2. For both CEN4 and WENO5 configurations, the LES model is based on a Turbulent Kinetic Energy

(TKE) 1.5 turbulence scheme [Cuxart et al., 2000].

The equations in YALES2 are discretized with a fourth-order central scheme in space and a fourth-order Runge-Kutta scheme in time (TFV4A) [Kraushaar, 2011]. The subgrid turbulence model for the reference YALES2 simulation is the Wall-Adaptative Local Eddy-Viscosity (WALE) model [Nicoud and Ducros, 1999] since it is known to be more adapted to represent turbulent flows near walls than the model due to [Smagorinsky, 1963]. Comparison between WALE and Smagorinsky's subgrid turbulence models is performed in Sect. 5.2, since several LES studies reported in the literature used the Smagorinsky's model [Camelli et al., 2005, Santiago et al., 2010, Dejoan et al., 2010].

AVBP uses a third-order in space and time, explicit, two-step Taylor-Galerkin (TTGC) scheme or a second-order in space and time Lax-Wendroff (LW) scheme. For the reference AVBP simulation, TTGC is used since it is supposed to be more precise and less dissipative than LW [Colin and Rudgyard, 2000]. Comparison between LW and TTGC simulations is performed in Sect. 5.2; subgrid turbulence is modelled by WALE as in the reference YALES2 simulation. Comparison between WALE and Smagorinsky's models is also performed for the LW configuration in Sect. 5.2.

4 Large-Eddy Simulations (LES) of the MUST Trial 2681829

4.1 Computational Grids

The same computational grid cannot be used by the three codes since AVBP and YALES2 are unstructured solvers, whereas Meso-NH is a structured solver. Two different grids are therefore used for the reference simulations, a structured grid for Meso-NH on the one hand, and a unstructured grid for AVBP and YALES2 on the other hand. Each grid allows to take advantage of the best features and performance of the different code architectures, resulting from a trade-off between accuracy, computational cost and memory issues that is different for each LES code. Computational costs are indicated in Table 2.

The MUST trial 2681829 was simulated for Meso-NH over a computational domain of 300-m long, 300-m wide and 40-m high. The height of the computational domain is about 15 times the container height (2.54 m) following recommendations by [Franke et al., 2011]. With these dimensions, the regular Cartesian structured grid is constituted of 135 million hexahedra. The same horizontal and vertical resolutions (0.2 m) are used from the surface to 10 m. Above 10 m, the vertical resolution decreases with a geometrical progression (ratio of 1.08 with the constraint of keeping the vertical resolution below 1 m). Flat ground is boundary-fitted and containers are modelled by an IBM [Mittal and Iaccarino, 2005] recently implemented and validated by [Auguste et al., 2019]. Numerical tests (not shown here) have demonstrated that a minimum resolution of the container with ten points per side is required when using the IBM, which is satisfied in the present study (the 2.42-m container width is discretized with a 0.2 m resolution with Meso-NH).

For AVBP and YALES2, the computational domain is meshed with 71 million tetrahedra; the resolution is equal to 0.3 m from the surface until 10 m, and coarsened vertically up to a resolution

equal to 1 m at the upper boundary condition. The grid is unstructured and boundary-fitted. Sensitivity of the YALES2 results to the grid is investigated, by changing the type of elements (hexahedra instead of tetrahedra) and the finest resolution near the source (0.2 m instead of 0.3 m, corresponding to a new mesh of 246 million hexahedra), to have a grid that is closer to that of Meso-NH simulations to go further into the model-to-model comparison.

The mesh resolutions tested in the present study are among the finest resolutions found in the literature, which typically range from 16 cm in camelli2005 (camelli2005) to 60 cm in milliez2007 (milliez2007). High-resolution LES is useful to capture the small-scale turbulent structures induced by the presence of containers in the MUST test case.

4.2 Initial and Boundary Conditions

One challenge in CFD simulation of near-field pollutant dispersion is the treatment of large-scale atmospheric forcing. In field-scale experiment such as MUST, there is usually a limited amount of information to represent the level of details present in the actual inflow conditions. So as in previous MUST studies and as in many atmospheric pollution dispersion models, the inlet and initial wind fields are imposed using a mean horizontal upstream wind, which follows a logarithmic evolution with the altitude z [Monin and Obukhov, 1954]. This profile is only valid in neutral conditions and in the surface layer, which is sufficient in this near-neutral MUST trial, where we focus on the near-surface flow within the container canopy. The mean horizontal upstream wind $\bar{u}(z)$ reads

$$\bar{u}(z) = \frac{u_*}{\kappa} \ln \left(1 + \frac{z}{z_0} \right), \quad (7)$$

where z_0 (m) is the surface roughness length equal to 0.045 m according to observations [Yee and Biltoft, 2004]; κ is the von Kármán constant equal to 0.4; and u_* (m s^{-1}) is the friction velocity. The formulation of $\bar{u}(z)$ is semi-empirical in the sense that z_0 and u_* are calculated based on horizontal wind speed data available at the upstream tower S at different heights (1.15, 4, 8 and 16 m); u_* is estimated through a least-square regression of Eq. (7) to these data. The resulting vertical profile (dashed line) is presented in Fig. 2 along with the measurements used for regression (circles). The optimized value of u_* is equal to 0.715 m s^{-1} , which is in good agreement with the measurement 0.680 m s^{-1} obtained from a sonic anemometer at $z = 1.15 \text{ m}$ near tower S. The resulting profile is used as initial condition and as lateral boundary condition in the LES.

Even though the upstream wind is subject to temporal variability, only the mean profile $\bar{u}(z)$ with $u_* = 0.715 \text{ m s}^{-1}$ and the mean angle $\alpha = -41$ (corresponding to a south-southwest wind) are imposed at the inlet of the computational domain. The reason is two-fold: i) the turbulence generation becomes rapidly controlled by the containers within the canopy, which strongly modifies the near-surface flow topology, and the experimental sensors of interest are located after this transition; ii) the three codes have a very different treatment for turbulence injection, which would introduce a discrepancy detrimental for the comparison of the three codes.

In AVBP and YALES2, the boundary conditions for both ground and containers are a law-of-the-wall based on a viscous length [Schmitt et al., 2007]. In Meso-NH, the ground surface is

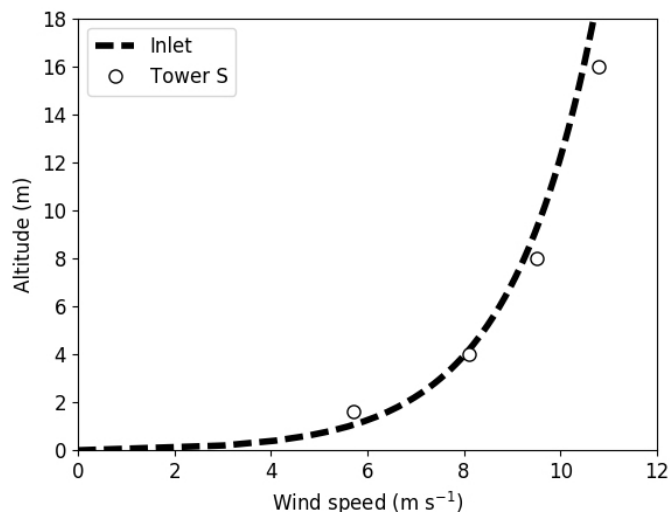


Figure 2: Vertical profile of the horizontal mean wind speed $\bar{u}(z)$ at tower S (tower location is indicated in Fig. 1). Comparison between experimental data (symbols) and the corresponding fitted profile (dashed line) obtained using Eq. (7) for $u_* = 0.715 \text{ m s}^{-1}$. The fitted profile is used as initial condition and as lateral boundary condition in the LES.

described with the SURFEX surface scheme [Masson et al., 2013], which computes the Reynolds stress based on the roughness length z_0 . In AVBP, characteristics-based NSCBC (Navier-Stokes Characteristics Boundary Conditions) are used at inlet and outlet to properly handle acoustics [Poinsot and Lele, 1992, Granet et al., 2010].

The tracer release starts 15 seconds after the initialisation of the simulation. This delay allows to establish the turbulence induced by the obstacles. 15 additional seconds are then needed to establish the plume in the domain. Finally, 200 more seconds are simulated to obtain converged statistics. In the following, time 0 s corresponds to the tracer release time. Examples of instantaneous flow and tracer concentration fields are given in Fig. 3. Small-scale turbulent structures induced by the containers are visible in Fig. 3a, where flow acceleration in-between the containers and stagnation areas can be observed. The resulting turbulent tracer concentration field is presented in Fig. 3b, where local tracer concentration can reach 10 ppm in the first container lines and columns near the emission source.

4.3 Validation Metrics

LES model performance is evaluated using the standard statistical metrics for air quality model evaluation [Chang and Hanna, 2004], which were also used in previous MUST studies [Hanna et al., 2004, Milliez and Carissimo, 2007, Donnelly et al., 2009, Antonioni et al., 2012, Kumar et al., 2015]. These metrics compare the tracer concentrations extracted from the simulations with those measured experimentally in terms of normalized mean square error (NMSE), fractional bias (FB), fraction of predictions within a factor of two of observations (FAC2), geometric mean bias (MG) and geometric

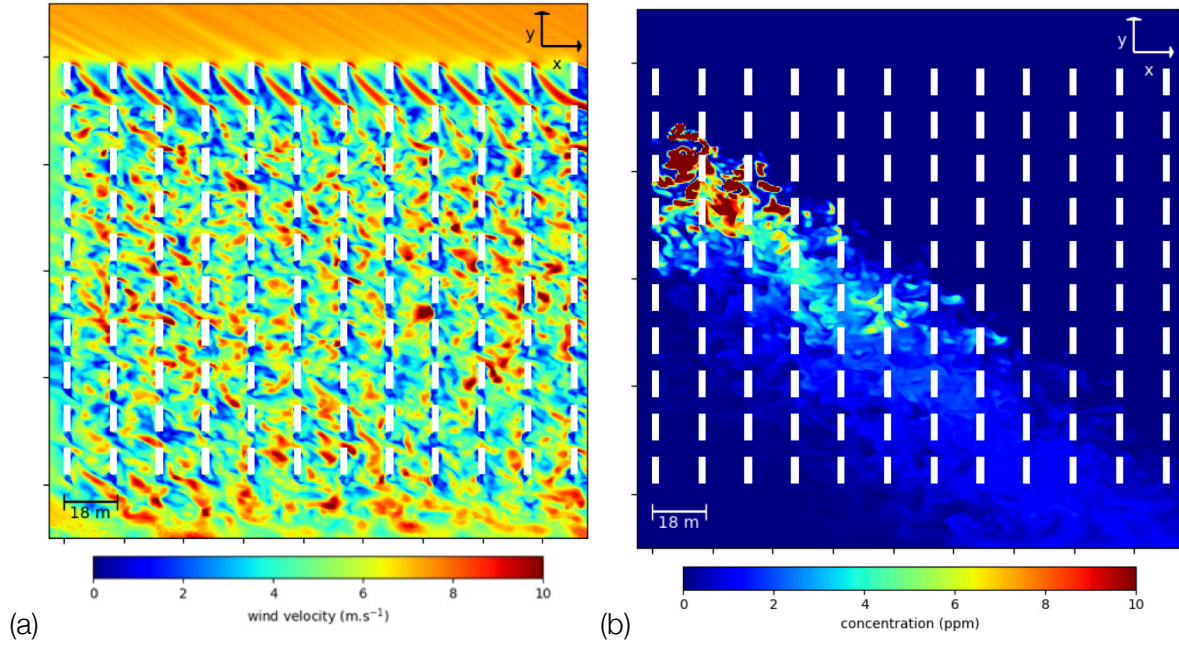


Figure 3: Examples of instantaneous horizontal (a) wind speed magnitude (m s^{-1}) and (b) tracer concentration (ppm) obtained with AVBP at $z = 1.6$ m and at time instant 47 s. White rectangles represent containers.

variance (VG):

$$\text{NMSE} = \frac{\overline{(C_o - C_s)^2}}{\overline{C_o} \overline{C_s}}, \quad (8)$$

$$\text{FB} = \frac{(\overline{C_o} - \overline{C_s})}{0.5(\overline{C_o} + \overline{C_s})}, \quad (9)$$

$$\text{FAC2} = \text{fraction of data that satisfies } 0.5 \leq \frac{C_s}{C_o} \leq 2.0, \quad (10)$$

$$\text{MG} = \exp(\overline{\ln C_o} - \overline{\ln C_s}), \quad (11)$$

$$\text{VG} = \exp\left[\overline{(\ln C_o - \ln C_s)^2}\right], \quad (12)$$

where C_o and C_s are the observed and simulated concentrations, and the overbar denotes the mean (time-averaged) value over the dataset. FB and MG measure the mean relative bias and are an indicator of systematic errors. NMSE and VG measure the mean relative scatter and indicate both systematic and random errors. A perfect model would have NMSE and FB equal to 0; FAC2, MG and VG equal to 1. The “acceptable” values that take these metrics for an acceptable model according to [Chang and Hanna, 2004] are given in Table 4.

Observed and simulated concentrations are compared using the same sample period of 0.2 s. A time average is then performed on these concentration datasets to compute the statistical met-

rics at each sensor located at $z = 1.6$ m throughout the array of containers (circles in Fig. 1). Metrics such as MG and VG are very sensitive to low concentration values. To overcome this issue, [Chang and Hanna, 2004] recommend to assume a minimum threshold to calculate the metrics. This threshold is here taken as the instrument detection threshold (0.04 ppm): any instantaneous value of the time series that is less than 0.04 ppm is set equal to 0.04 ppm for both observations and simulations. MG and VG metrics could be improved by considering a minimum threshold of 0.1 ppm [Milliez and Carissimo, 2007, Thouron et al., 2020], but this possibility was rejected here to remain consistent with the experiment. This choice implies that in practice, 15 of the 40 sensors are discarded from the analysis since the recorded concentration at these sensors is always below the minimum threshold [Thouron et al., 2020]. In the following, all time-averaged statistics and fields are calculated after plume stabilisation over the period [15; 215 s].

The Pearson correlation coefficient R and the spatial standard deviation σ_C of the (observed or simulated) tracer concentration C are also computed:

$$\sigma_C = \sqrt{\overline{C^2} - (\overline{C})^2}, \quad R = \frac{\overline{C_o C_s} - \overline{C_o} \overline{C_s}}{\sigma_{C_o} \sigma_{C_s}}. \quad (13)$$

Besides time-averaged quantities, concentration fluctuations are also important and accessible with LES. One way to highlight them is to analyse the results in terms of percentiles rather than absolute maximum values [Tominaga and Stathopoulos, 2013]. A specific concentration percentile can be directly extracted from the LES, which is an advantage compared to RANS. In the following, the 99th percentile of concentration time series at each sensor location is computed along with the maximum and the temporal standard deviation.

4.4 Inventory of LES runs

A pool of eight LES was carried out using eight different LES models to evaluate the variability in the LES model response. Table 3 summarizes the different reference and sensitivity LES analysed in Sect. 5. AVBP, Meso-NH and YALES2 were first used with their reference set-up to simulate the MUST trial 2681829; results are presented in Sect. 5.1. The sensitivity of the LES results to other possible user's choices was also tested in each code, such as the computational grid, the subgrid turbulence model and the advection scheme; results are presented in Sect. 5.2. An analysis of the uncertainty in the LES model response is also provided. Computational costs are discussed in Sect. 5.3. The reader shall refer to the complementary technical report by [Thouron et al., 2020] for complementary explanations on the LES strategy and results.

5 Results and Discussions

5.1 Validation of Reference Simulations

Reference LES results (configurations named MNH-IBM_reference, Y2_reference and AVBP_reference and presented in Table 2) are compared to measurements in terms of wind speed and tracer con-

Table 3: Inventory of reference and sensitivity LES presented in this study for the MUST trial 2681829 with Meso-NH, YALES2 and AVBP. The reference runs correspond to the numerical configurations presented in Table 2. In bold are indicated the components that change in the sensitivity tests.

Codes	Run	Advection scheme	Turbulence scheme	Grid
Meso-NH	MNH-IBM_reference	WENO5	TKE 1.5	135 million hexahedra
	MNH-IBM_cen4	CEN4	TKE 1.5	135 million hexahedra
YALES2	Y2_reference	TFV4A	WALE	71 million tetrahedra
	Y2_hexa	TFV4A	WALE	246 million hexahedra
	Y2_smago	TFV4A	Smagorinsky	71 million tetrahedra
AVBP	AVBP_reference	TTGC	WALE	71 million tetrahedra
	AVBP_lw	LW	WALE	71 million tetrahedra
	AVBP_lw_smago	LW	Smagorinsky	71 million tetrahedra

centration for validation purpose.

5.1.1 Micro-scale Meteorology

Figure 4 presents the mean horizontal wind field at $z = 1.6$ m for (a) Meso-NH, (b) YALES2 and (c) AVBP. Left panels represent the mean horizontal wind speed. Right panels represent the percentage frequency distribution of wind speed and direction, also referred to as wind rose, which is obtained by taking the time-averaged wind speed and direction values at all grid cells at $z = 1.6$ m to estimate the percentage frequency distribution. Recall that the north direction corresponds to an angle of -30 in the x - y frame presented in Fig. 1 and that the incident wind flow blows from the south-southwest direction (-41 , Table 1) that is indicated using a red arrow in the wind roses.

For the three codes, left panels in Fig. 4 show that the incident flow is significantly slowed down by the containers. Already, a decrease in the wind speed is noticeable upstream of the entrance of the container array due to the effect of the containers acting as obstacles to the flow. There is also a significant flow acceleration in the space between the containers within the first two lines (8–9) and columns (K–L) of containers. In the present MUST trial, the wind direction and the container array diagonal are almost aligned, emphasizing this channeling effect, which is stronger for Meso-NH than for YALES2 and AVBP. Downstream, i.e. after the first three lines and columns of containers, a similar flow is obtained for the three codes: the wind is globally slowed down compared to the inlet wind (about 4 m s^{-1} at $z = 1.6$ m to be compared to 6 m s^{-1} for the inlet wind). In this zone, the turbulent boundary layer induced by the container-induced roughness is fully established.

Figure 5 presents the mean vertical profile of the wind speed and direction at the central tower T that is located in the downstream area (Fig. 1). Results show that the simulated profiles (solid lines)

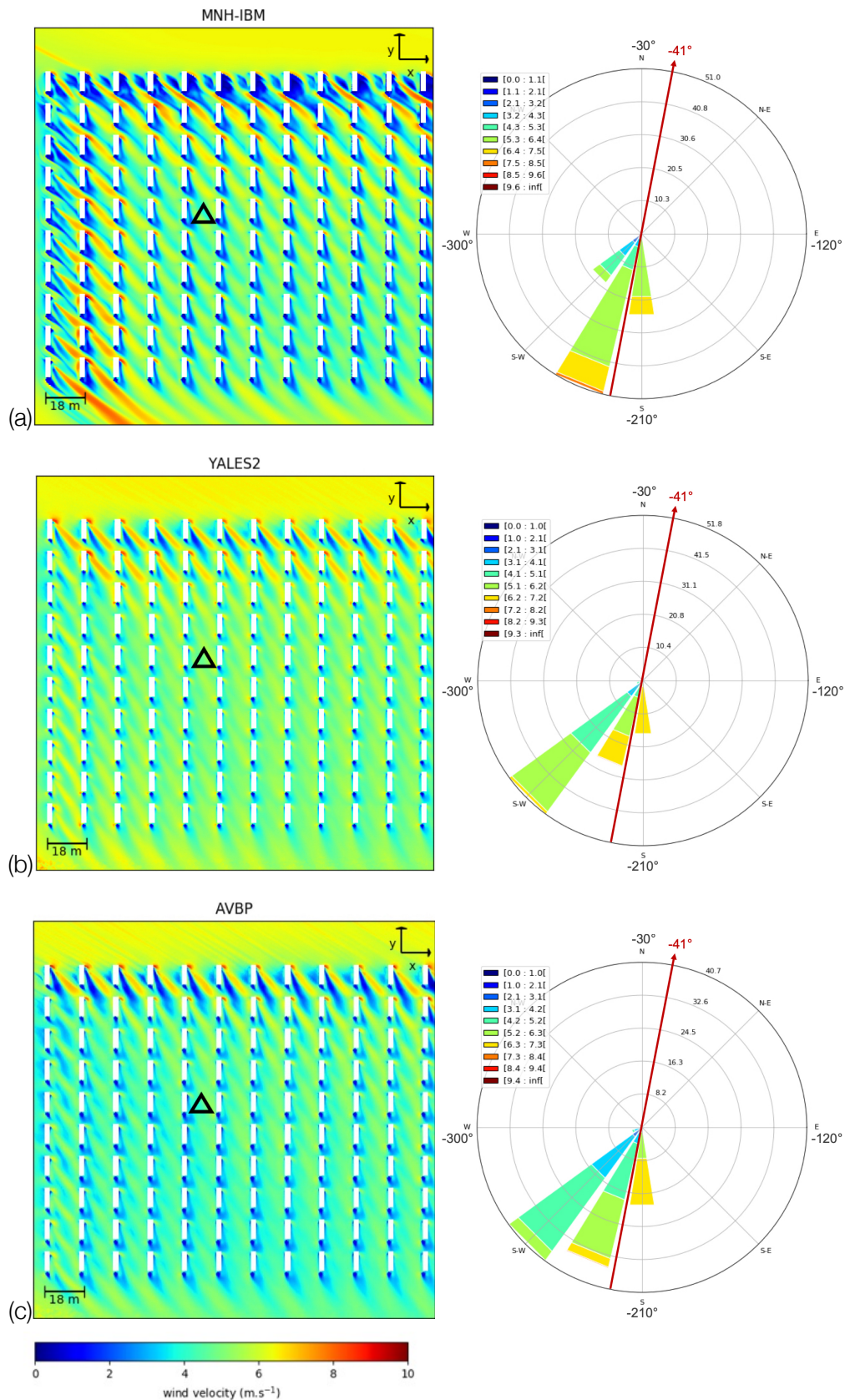


Figure 4: Mean horizontal wind at $z = 1.6$ m for reference (a) Meso-NH, (b) YALES2 and (c) AVBP simulations named MNH-IBM_reference, Y2_reference and AVBP_reference. Left panels: wind speed magnitude (m.s^{-1}); white rectangles represent containers; black triangle represents the central tower T. Right panels: wind roses representing the percentage frequency distribution of wind speed (m.s^{-1}) and direction ($^\circ$); the percentage frequency is indicated with the grey circles: the larger the circle radius, the larger the percentage frequency. The direction indicated in the wind roses corresponds to the direction from which the wind is blowing: the north direction corresponds

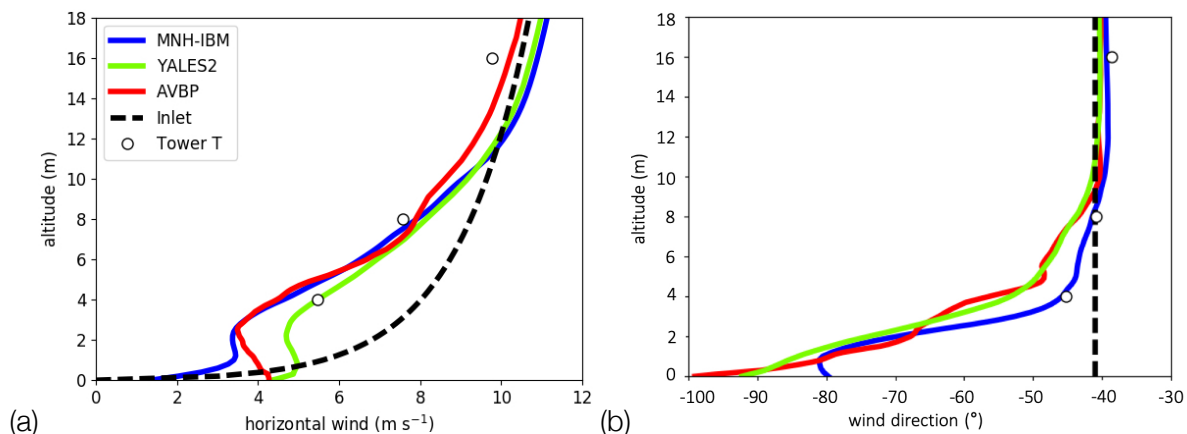


Figure 5: Mean horizontal (a) wind speed and (b) wind direction profiles at the central tower T. Comparison between observations (circles) and reference LES (solid lines): Meso-NH (blue), YALES2 (green) and AVBP (red). The inlet profile is also indicated (dashed vertical line corresponding to -41°). For the wind direction, -30 corresponds to a wind blowing from the south to the north direction and -120 to a wind blowing from the west to the east direction (see wind roses in Fig. 4).

are coherent with the available measurements (symbols). Figure 5a confirms that the inlet flow (black dashed line) is significantly slowed down by the containers, whose influence is noticeable until about $z = 10$ m. Very close to the ground, the horizontal wind speed in YALES2 and AVBP is higher compared to the inlet condition and to Meso-NH. The different treatments of wall boundaries on the containers between the three codes may induce this discrepancy: immersed wall boundary form Meso-NH versus law-of-the-wall treatment for AVBP and YALES. Above 12 m, Meso-NH and YALES2 present an increase in the horizontal wind speed compared to the inlet profile (less than 0.5 m s^{-1}) as found in [König, 2014]. In contrast, the experimental data available at $z = 16$ m indicate a slight decrease. This slowdown is partly captured by AVBP.

Results in Figure 5b show that above the containers, the wind direction slightly deviates from the initial state in Meso-NH in coherence with the observation (circle symbol at $z = 16$ m). This deviation was also found in [Dejoan et al., 2010] for different inlet wind directions. With YALES2 and AVBP, the deviation is less pronounced at this altitude.

Results in Figure 5b also show that near the ground there is a shift in the simulated flow direction with a wind blowing from a more western direction; this shift is stronger for AVBP and YALES than for Meso-NH. This is consistent with the wind roses presented in the right panels of Fig. 4, which present more global wind flow statistics since wind roses are generated using information from the whole computational domain. For Meso-NH, the wind direction ranges from south to south-west within the container array. About 50% of the data feature a south-southwest wind for which the wind speed is mainly above 5 m s^{-1} (green-to-orange colors in the wind roses). This wind direction corresponds to the inlet flow conditions (red arrow) that can be considered as moderate wind conditions (calm conditions in-between the containers would correspond to wind speed below 2 m s^{-1}). But, less than 20% of the Meso-NH data feature a southwest wind (corresponding to the vertical alignment of the containers) with calmer conditions, i.e. the wind

speed is mostly between 4 and 5 m s⁻¹. For YALES2 and AVBP, more than 40% of the data feature such a southwest wind, indicating a more significant impact of the containers on the flow dynamics than for Meso-NH. Calmer wind conditions are also noticed in this direction compared to the south-southwest direction.

5.1.2 Tracer Dispersion

Figure 6 presents the mean horizontal tracer concentration at $z = 1.6$ m for (a) Meso-NH, (b) YALES2 and (c) AVBP; it also provides comparison with the observed mean concentration at each sensor location (colored circles, where the color corresponds to the observed concentration). Left panels provide results for the reference configurations (which are associated with the mean horizontal wind field results presented in Fig. 4). Right panels provide results for some of the sensitivity configurations that will be analysed in Sect. 5.2. Most sensors are far from the emission source, in areas where the tracer concentration is low. For 15 sensors, this concentration is even below the 0.04-ppm threshold and these sensors are removed from the statistical analysis (Sect. 4.3). Only few sensors (e.g. sensor 9, Fig. 1) are in the area where the tracer concentration exceeds a few ppm; this is a limitation of the present MUST trial.

Reference results show that the shape of the simulated time-averaged plume differs between the three codes. In the Meso-NH simulation, the container array does not significantly modify the flow structure due to the strong channeling effect, so there is no significant lateral and vertical plume spread; the mean concentration remains very high along the plume centreline. In contrast, the plume shape simulated by AVBP and YALES2 presents a deviation of its centreline direction towards the K-L columns of containers (AVBP features the largest deviation). This plume deflection is consistent with the wind roses presented in Fig. 4 indicating a wind shift towards the south-west direction for AVBP and YALES2. This plume deflection is consistent with the literature [Milliez and Carissimo, 2007, König, 2014] and the measurements.

In complement, Fig. 7 represents the tracer concentration time series at sensors 5, 9, 16 and 31 (sensors 5 and 9 are located on the first column of sensors, sensor 16 on the second column and sensor 31 on the fourth column, Fig. 1). In Meso-NH, since there is no significant deviation of the plume with respect to the inlet wind, the tracer concentration tends to be overestimated in the plume centreline (at sensors 9, 16 and 31) and to be underestimated on the plume flanks (at sensor 5). This is particularly true near the source: at sensor 9 the mean simulated tracer concentration obtained with Meso-NH (7.0 ppm) differs from measurements (4.2 ppm). By capturing the plume centreline deviation, the tracer concentration decreases more rapidly downstream for AVBP and YALES2 than for Meso-NH. AVBP (3.8 ppm) and YALES2 (5.1 ppm) provide a much improved tracer concentration prediction at sensor 9 than Meso-NH. This is also the case at sensor 5. Further downstream, Meso-NH well reproduces the observed background tracer concentration at sensor 31: the mean concentration is 0.94 ppm for observations and 1.21 ppm for Meso-NH, while it is underestimated (below 0.56 ppm) for AVBP and YALES2. The plume deflection may be too strong in AVBP and YALES2 compared to reality.

Table 4 presents a more global viewpoint through the statistical metrics of [Chang and Hanna, 2004]

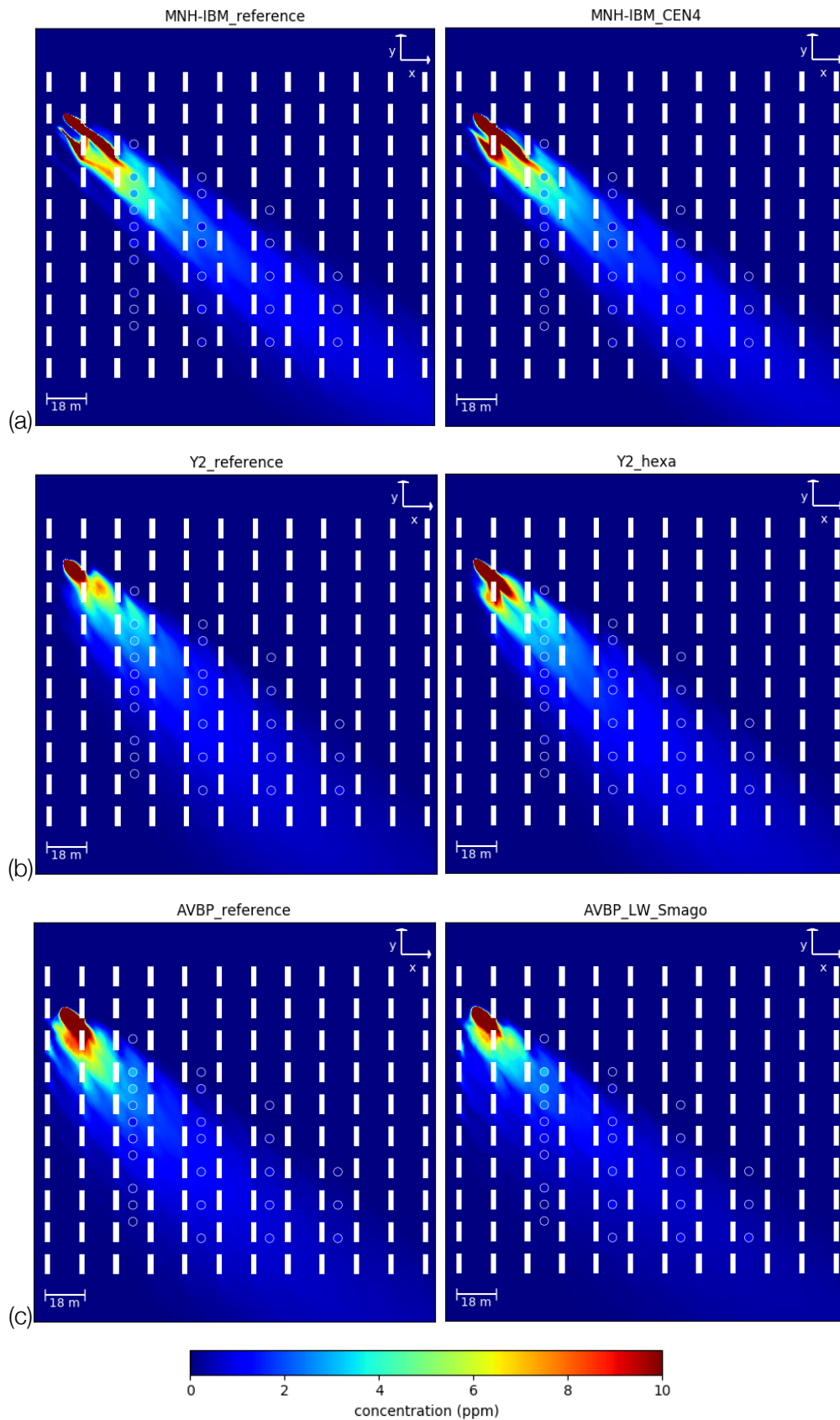


Figure 6: Mean horizontal tracer concentration (ppm) at $z = 1.6$ m for (a) Meso-NH, (b) YALES2 and (c) AVBP simulations. Left panels correspond to reference simulations named MNH-IBM_reference, Y2_reference and AVBP_reference. Right panels correspond to some sensitivity simulations named MNH-IBM_cen4, Y2_hexa and AVBP_lw_smago. The observed mean concentration (ppm) at the sensor locations is also given by the symbol colors (circles) using the same color map. White rectangles represent containers.

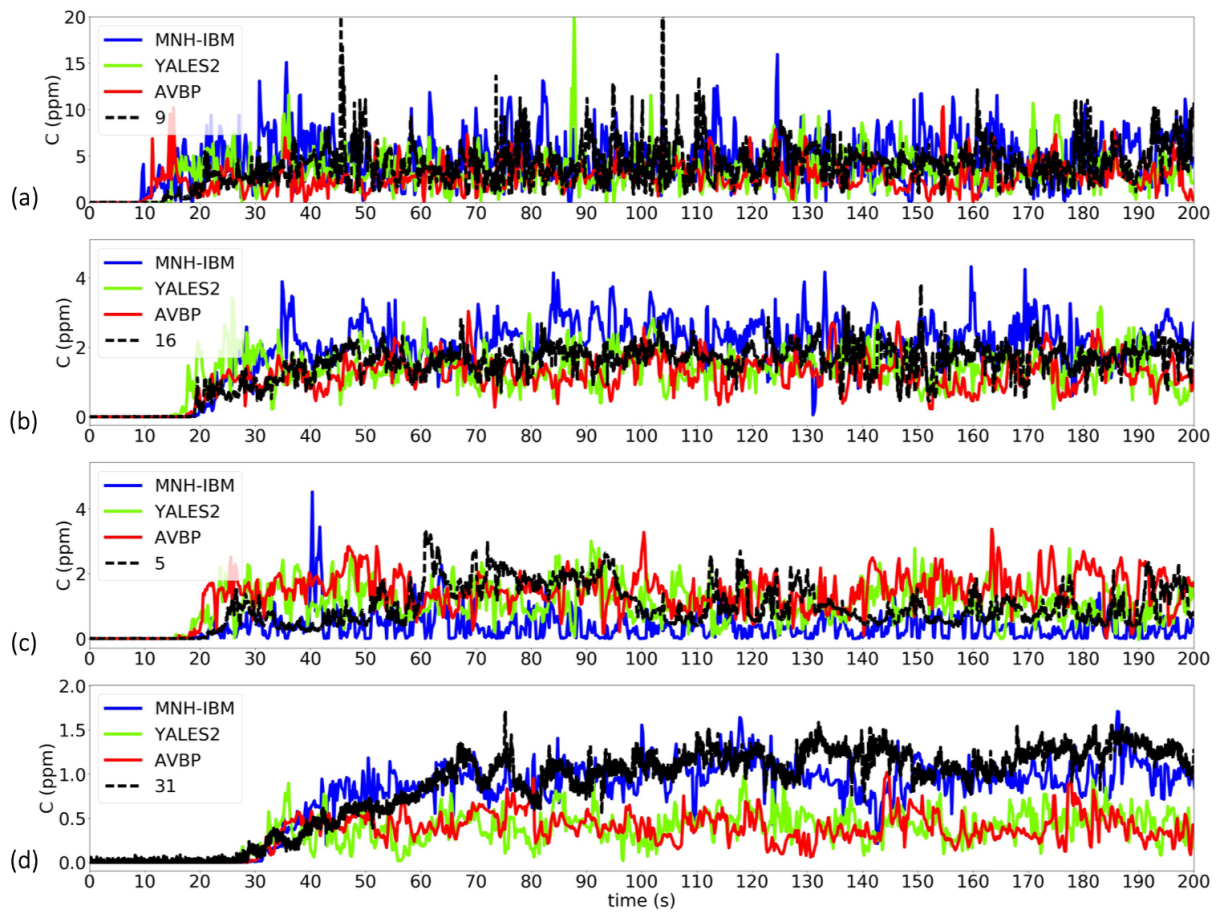


Figure 7: Time series of tracer concentrations (ppm) at four different sensors: (a) 9, (b) 16, (c) 5 and (d) 31 (red circles in Fig. 1). Measurements are represented as dashed lines; reference LES results are indicated as solid lines: red for AVBP, blue for Meso-NH and green for YALES2.

Table 4: Standard statistical measures (Sect. 4.3). Perfect values, acceptable values and values extracted from Meso-NH, YALES2 and AVBP simulations in reference and sensitivity configurations. The best configuration for each LES code is indicated in bold. RANS results reported in the literature are given on an indicative basis.

Model/LES	NMSE	FB	FAC2	MG	VG
Perfect	0	0	1	1	1
“Acceptable” <small>[Chang and Hanna, 2004]</small>	<4	Between -0.3 and 0.3	> 0.5	Between 0.7 and 1.3	<1.6
MNH-IBM_reference	0.1162	-0.34	0.64	1.25	1.95
MNH-IBM_cen4	0.0704	-0.27	0.60	1.44	2.58
Y2_reference	0.0123	-0.11	0.76	1.24	1.68
Y2_hexa	0.0091	-0.10	0.76	1.30	1.62
Y2_smago	0.0145	0.12	0.76	1.41	1.73
AVBP_reference	0.0065	-0.08	0.56	1.22	2.18
AVBP_lw	0.0021	0.05	0.84	1.33	1.51
AVBP_lw_smago	0.0004	-0.02	0.72	1.15	1.59
Literature/RANS					
<small>[Milliez and Carissimo, 2007] (20 trials)</small>	1.95	-0.08	0.70	1.09	1.84
<small>[Donnelly et al., 2009] (only 2 neutral trials)</small>	1.50	-0.14	0.57	1.19	5.10
<small>[Kumar et al., 2015] (only 2 neutral trials)</small>	0.23–0.41	0.23–0.47	0.46–0.67	1.69–2.07	1.94–2.28

computed for all sensors following the methodology presented in Sect. 4.3. Results show a good agreement of all the metrics with observations. NMSE is very low for the three codes compared to the acceptable value and RANS results. FAC2 (ranging between 56% for AVBP_reference to 76% for Y2_reference) is well above the 50% acceptable value for the three codes. The three reference configurations feature a negative FB, meaning that the LES models tend to overestimate tracer observations. FB is within the acceptable range except for Meso-NH, which features a FB close to the acceptable threshold of -0.3, meaning that Meso-NH overestimates tracer concentrations in a larger extent than AVBP (FB equal to -0.08) and YALES2 (FB equal to -0.11). MG and VG do not satisfy the range of acceptable values for the three codes. These metrics are very sensitive to low tracer concentration values, which appear at some sensors far away from the plume centreline. This may indicate that the LES codes have some difficulty in capturing low background tracer concentrations in an accurate way.

In coherence with NMSE, FAC2 and FB metrics, the scatter plots of the observed versus simulated concentrations presented in Fig. 8 for several statistics (mean, standard deviation, 99th percentile and maximum, Sect. 4.3) demonstrate the consistency among the reference LES results obtained for the three codes. Correlation coefficients are always higher than 0.85 for the three codes, showing their ability to represent tracer concentration fluctuations. Higher tracer concentration values (above 1 ppm) are better represented by the three codes but usually overestimated, especially for Meso-NH. The highest simulated and observed 99th percentiles and maximum values in the three codes are all obtained at sensor 9. The 99th percentile (respectively the maximum) is equal to 9.9 ppm (respectively 23.1 ppm) for measurements, 16.7 ppm (respectively 21.7 ppm) for Meso-NH, 10.1 ppm (respectively 15.4 ppm) for YALES2, and 14.5 ppm (respectively 24.1 ppm) for AVBP.

5.1.3 Discussion

The three LES codes – AVBP, Meso-NH and YALES2 – provide good tracer concentration predictions, especially for high values, which is important for operational application where there is a need to go beyond mean prediction and to assess dose exposure. These information can be quantified by LES since they directly evaluate fluctuations (Fig. 3) and even percentiles of concentration, which is an advantage over RANS. Table 4 also indicates the statistical metrics obtained with RANS simulations presented in the literature, for twenty MUST trials selected by [Yee and Biltoft, 2004] for [Milliez and Carissimo, 2007] on the one hand, for the subset of two neutral trials for [Donnelly et al., 2009] and [Kumar et al., 2015] on the other hand; in both cases, the present trial 2681829 is included in the results. Results confirm the consistency between LES and RANS simulations of the MUST trial already observed in [Santiago et al., 2010] and [Dejoan et al., 2010], validating the multi-model LES configurations used in this study.

The most significant differences between the three LES codes appear within the first container lines, near the ground, which can be considered as the transition zone between an open-terrain plume to an array plume. Unfortunately, no measurement is available below $z = 4$ m. There is thus no way to discriminate the performance of the different models for the wind flow prediction near the

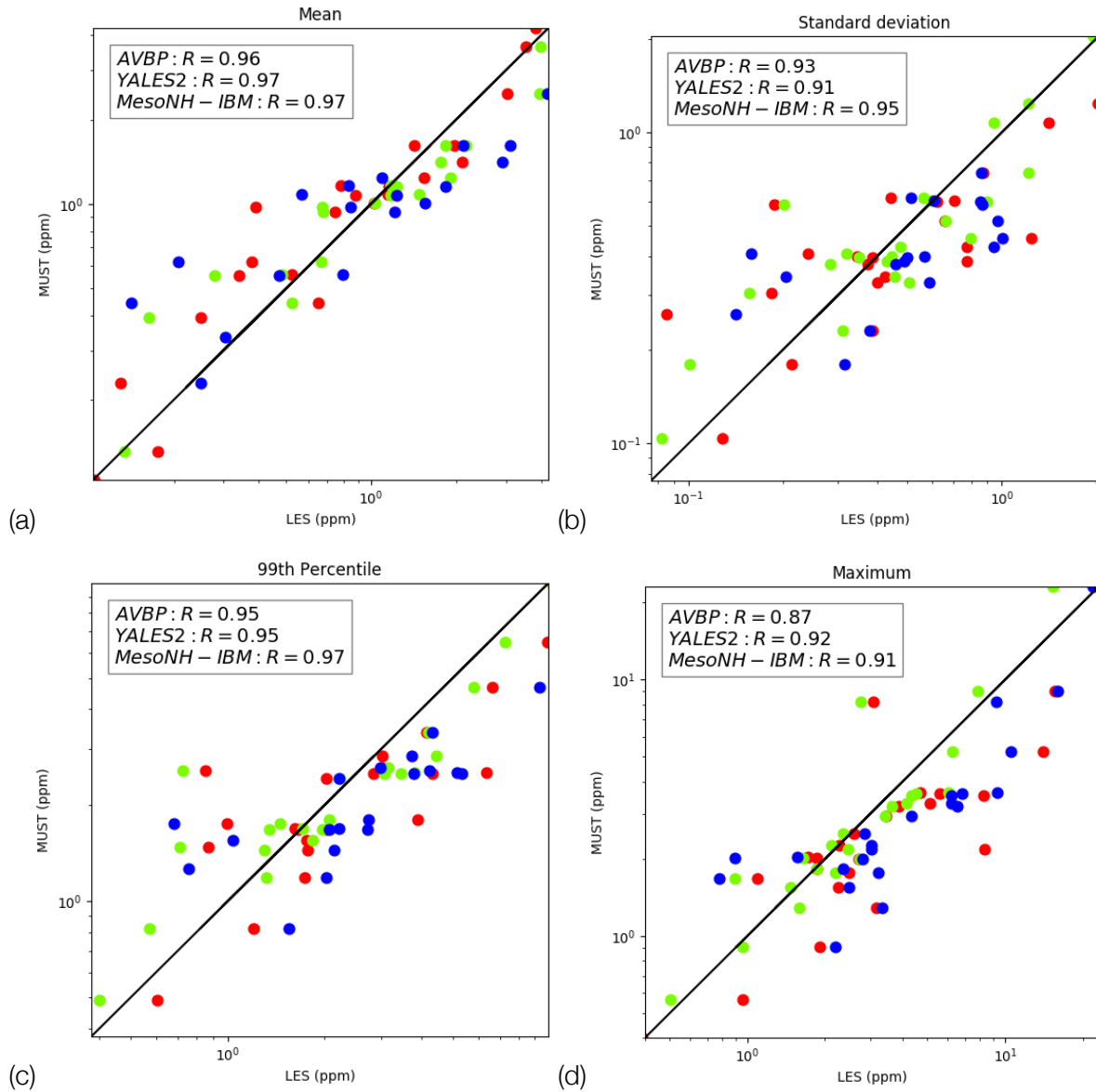


Figure 8: Scatter plots of measured (x -axis) versus simulated (y -axis) statistics: (a) temporal mean, (b) standard deviation, (c) 99th percentile and (d) maximum tracer concentration at each sensor for the three LES codes in their reference configurations: in blue for Meso-NH, in green for YALES2 and in red for AVBP. The correlation coefficient R is indicated for each code and for each statistics.

ground. This is a limitation of the MUST field campaign for model validation. Using unmanned aerial systems or a scanning lidar in future field campaigns could be helpful to explore more extensively the plume near the emission source, and to provide more informative data [Reymann et al., 2018, Clements et al., 2018]. Data assimilation algorithms can even be used to optimize observation network [Mons et al., 2017].

Moreover, a detailed analysis of the wind time series at the main tower T (not shown here but presented in auguste2019, auguste2019, for Meso-NH only) showed good agreements between Meso-NH and observations at $z = 4$ and 8 m, but not at 16 m, where the LES does not feature enough fluctuations, certainly due to the absence of inlet turbulence. This confirms that this study is relevant for analysing the tracer dispersion within the container canopy only. This absence of inlet turbulence could also explain the overestimation of high values of tracer concentration (above 1 ppm) in the LES. Improving the representation of large-scale atmospheric forcing is expected to improve the micro-scale LES model predictions within the container array [García-Sánchez and Gorlé, 2018, Lamberti et al., 2018].

The present comparison between three LES codes shows that relatively similar results can be obtained despite their intrinsic differences, and despite the fact that each code was used outside of its usual applications and scales. This highlights the reliability of the present LES results.

5.2 Sensitivity Study For Multi-Model Variability Estimation

Section 5.1 shows that the three LES codes provide very consistent results. It can be noted, however, that important similarities are more particularly shared between AVBP and YALES2 simulations. Of course, this may be due to the similarity between computational choices of AVBP and YALES2: same subgrid turbulence model (WALE), same boundary conditions for ground and containers, same computational grid. Tests have been carried out to analyse further the sensitivity of the LES results to the user's modelling choices and to perform an extensive model-to-model comparison.

Standard statistical metrics results obtained for all sensors for the sensitivity simulations are presented in Table 4 along with reference results. To go further into the analysis and to identify where there are differences between the reference and the sensitivity simulations, Table 5 presents the FAC2 values obtained for two groups of sensors (among the 25 sensors retained in this study for model evaluation, Sect. 4.3): i) a group of near-source sensors where high tracer concentrations (above 1 ppm) are observed in the MUST dataset (10 red dots in Fig. 9); and ii) a group of sensors where the observed tracer concentration is significantly lower (below 1 ppm) in the MUST dataset (15 blue dots in Fig. 9). The objective is to evaluate the performance of the LES models to predict local concentrations near the emission source (local FAC2), and background concentrations further away from the plume centreline (background FAC2). For clarity purpose, this analysis is only presented here for the FAC2 since it is considered as a robust measure in air quality problems; the full analysis is given in [Thouron et al., 2020].

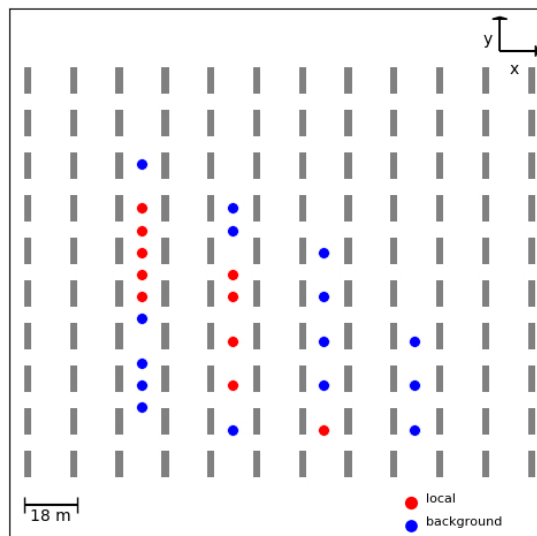


Figure 9: Map of the two sensor categories used in Table 5 to compute local and background FAC2 values. Red sensors represent near-source sensors (local FAC2), where the time-average tracer concentration is above 1 ppm in the observed dataset. Blue sensors represent background sensors (background FAC2), where this concentration is below 1 ppm.

5.2.1 Model-to-model Comparison

Sensitivity to Computational Grid. One of the possible reasons for the similarity observed between AVBP and YALES2 results is the identical computational grid. To investigate that point and evaluate the grid influence, a Cartesian hexahedra grid with a minimum spatial resolution equal to 0.2 m (same resolution and same type of grid element as in Meso-NH, Sect. 4.1) was generated for YALES2. This new configuration is named Y2_hexa (Table 3). Table 4 shows that very similar statistical metrics are obtained for both Y2_reference and Y2_hexa configurations. There is even no difference in terms of FAC2, even when separating local and background contributions (Table 5). The local FAC2 is equal to 100% and the background FAC2 is equal to 60%. Still, Fig. 6b indicates that there is a change in the averaged plume shape near the source. The plume structure obtained with Y2_hexa (right panel) is closer to that of the Meso-NH simulations than with Y2_reference (left panel). There is for instance, a stronger advection of the tracer along the plume centreline, but this change is not significant enough to explain the gap with Meso-NH results (Fig. 6a), for which the channeling effect is exacerbated.

Sensitivity to Subgrid Turbulence Model. The influence of the subgrid turbulence model in YALES2 is also tested by replacing WALE (Y2_reference) by Smagorinsky's formulation (Y2_smago). Tables 4–5 indicate that the statistical results obtained with YALES2 are very similar. The FAC2 metrics do not change as in the sensitivity study related to computational grid. Other metrics such as NMSE, MG and VG are not significantly modified compared to Y2_reference and Y2_hexa configurations. One difference is that FB changes its sign for Y2_smago and becomes positive, indicating that Y2_smago tends to underestimate the observations, while Y2_reference and Y2_hexa

Table 5: Local and background FAC2 metrics for all Meso-NH, YALES2 and AVBP reference and sensitivity simulations. The total FAC2 corresponds to the FAC2 given in Table 4. The best configuration for each LES code is indicated in bold.

Model	Local FAC2	Background FAC2	Total FAC2
MNH-IBM_reference	0.80	0.53	0.64
MNH-IBM_cen4	0.70	0.53	0.60
Y2_reference	1.00	0.60	0.76
Y2_hexa	1.00	0.60	0.76
Y2_smago	1.00	0.60	0.76
AVBP_reference	0.80	0.40	0.56
AVBP_lw	1.00	0.73	0.84
AVBP_lw_smago	1.00	0.53	0.72

tend to overestimate them. Another difference is that the 99th percentile is not located at sensor 9 unlike in the observation and in the reference simulations, but at the central tower T at $z = 8$ m. This is due to changes in the wind patterns near the ground, particularly between the J–K columns of containers, where the wind is found to decrease in Y2_smago. The Y2_hexa configuration is indicated as the best YALES2 LES model by considering all statistical metrics, especially NMSE and FB. Still, all YALES2 configurations are in a very narrow range and are not much sensitive to the tested LES components.

Sensitivity to Advection Schemes. Alternative advection schemes – CEN4 in Meso-NH (MNH-IBM_cen4) and LW in AVBP (AVBP_lw) – are tested.

For Meso-NH, the main difference between MNH-IBM_reference and MNH-IBM_cen4 is the diffusion induced by the numerical scheme, since the WENO5 scheme is intrinsically more dissipative and leads to a more diffuse and spread plume than with the CEN4 scheme. Figure 6a shows that the averaged plume shape is relatively similar for both Meso-NH simulations compared to that obtained with AVBP and YALES2. Still, results in show that the total FAC2 decreases to 60% for MNH-IBM_cen4 (instead of 64% for MNH-IBM_reference). There is a slight change in the recirculation zone induced by the J7 container between both Meso-NH simulations, which may explain the better local FAC2 obtained with MNH-IBM_reference (80%) than with MNH-IBM_cen4 (70%) in Table 5. Still, the local FAC2 remains still below the one obtained with YALES2 and AVBP (80 to 100%).

In AVBP, the LW scheme is known to be more diffusive than TTGC that was used in the reference simulation. AVBP_lw simulates tracer concentrations that are more in agreement with the observations than AVBP_reference. A larger number of sensors is included in the range of observations with a total FAC2 equal to 84% in AVBP_lw (instead of 56% in AVBP_reference). As shown in Table 5, this is due to a simultaneous improvement in the local and background tracer concentration representation in AVBP_lw compared to AVBP_reference: the local FAC2 changes from 80% to 100%, and the background FAC2 changes from 40% to 73%. An additional AVBP simulation

(AVBP_lw_smago) is performed by combining the LW scheme and Smagorinsky's model. This last simulation again improves the total FAC2 compared to AVBP_reference: the total FAC2 is equal to 72% and is thereby almost at the same level as for YALES2 configurations (76%). Table 5 indicates that AVBP_lw_smago gives a perfect local FAC2 (100%) as AVBP_lw, but the background FAC2 (53%) is less good than with AVBP_lw (73%). This makes AVBP_lw the best performing LES model in terms of local and background FAC2 metrics. The LW numerical scheme plays an important role in this performance. Remarkably, the change of the subgrid turbulence model does not have the same effect on the results for AVBP and YALES2.

Discussion. AVBP provides the best results in terms of background tracer concentrations (best background FAC2 equal to 73%), but also in terms of near-source tracer concentrations (best local FAC2 equal to 100% as for YALES2 configurations). The sensitivity simulations induce some small changes in the tracer dispersion and in the statistical metrics among the different codes and the different configurations. Still, in spite of the differences pointed out in this work, the LES results remain relatively stable for all tested settings, showing the robustness of the LES modelling strategy.

The following conclusions can be drawn. First, the choice of the numerical advection scheme is the most significant factor in the present sensitivity study when considering statistical metrics, but the choice of the computational mesh has shown some influence on the plume structure. Second, the best configurations for the three LES codes do not necessarily correspond to the reference configurations for the three codes: for AVBP the best configuration is the sensitivity simulation associated with the LW numerical scheme (AVBP_lw) and for YALES2 the best configuration is the sensitivity simulation associated with the hexahedra-type computational mesh (Y2_hexa). Only Meso-NH achieves its best performance in its reference configuration involving the WENO5 numerical scheme (MNH-IBM_reference). Third, the LES models show their ability to accurately represent the near-source wind flows and tracer concentrations with a local FAC2 ranging from 70% to 100% for all tested configurations. The background tracer concentrations are not represented as accurately with a background FAC2 ranging from 40% to 73%. This may be due to the simplification of the inlet boundary condition: accounting for the variability of the large-scale atmospheric forcing [Yamada and Koike, 2011, García-Sánchez et al., 2017, García-Sánchez and Gorlé, 2018, Lamberti et al., 2018, Defforge et al., 2019] may help at better representing the flow properties through the whole container array and at improving the background tracer concentration predictions. But this was beyond the scope of the present study, which focused on estimating the near-source multi-model variability.

5.2.2 Estimation of Multi-Model Variability

To go further into the assessment of the LES model quality, Fig. 10 presents the time-varying spread or “envelope” of the three best configurations (grey shaded area) obtained with Meso-NH, YALES2 and AVBP for (a) 25 sensors and (b) local sensors restricted to an area near the source where tracer concentrations are above 1 ppm (Fig. 9). The corresponding time series of the

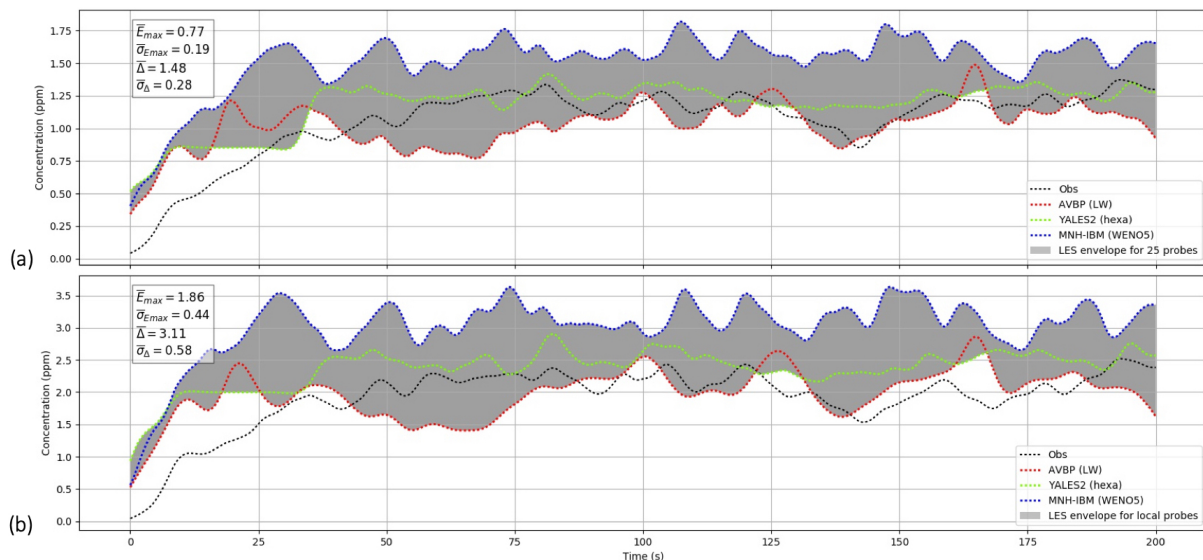


Figure 10: Time series of the best LES configurations, in blue for Meso-NH (MNH-IBM_reference), in green for YALES2 (Y2_hexa) and in red for AVBP (AVBP_lw), obtained for (a) 25 sensors and (b) local near-source sensors (red dots in Fig. 9).

observed tracer concentration is also presented (black dashed lines). The observed and simulated datasets are available at 0.2-s time intervals; a Hodrick-Prescott filter is applied to smooth out the signals and focus on long-term fluctuations, from which several statistics are extracted. First, we estimate the model error E_{max} with respect to the observations: for each time step over the 200-s period, E_{max} is estimated as the maximum distance between the model envelope (grey shaded area) and the observation; time-averaged statistics of this maximum distance (the mean value \bar{E}_{max} and the standard deviation $\bar{\sigma}_{E_{max}}$) are then derived. Second, we estimate the LES model variability as the width Δ of the multi-model envelope (grey shaded area) at a given time; time-averaged statistics of the model envelope (the mean value $\bar{\Delta}$ and the standard deviation $\bar{\sigma}_{\Delta}$) are then derived. The statistics $\{\bar{E}_{max}, \bar{\sigma}_{E_{max}}, \bar{\Delta}, \bar{\sigma}_{\Delta}\}$ are indicated in Fig. 10.

Results in Fig. 10 show that the observed signal is not systematically within the multi-model envelope, especially at local sensors. The LES models are found to slightly overestimate observed tracer concentrations over all sensors. This is consistent with negative FB found for most LES models, especially for Meso-NH, which features high negative FB around -0.3 (Table 4). This is also consistent with the fact that Meso-NH simulates a plume centreline that remains aligned with the inlet wind direction. The signals obtained with AVBP are the closest to the observation, confirming the best performance of the AVBP_lw configuration when looking at the standard statistical metrics (highest total, local and background FAC2; low positive FB).

Meso-NH corresponds to the upper limit of the envelope, while AVBP corresponds to the lower limit. The mean envelope width $\bar{\Delta}$ is equal to 1.48 ± 0.28 ppm when considering all sensors (Fig. 10a). When only looking at local sensors (Fig. 10b), the mean envelope width is more significant, it is equal to 3.11 ± 0.58 ppm. The multi-model variability is thereby on the order of magnitude of the observed mean concentration.

5.3 Computational costs

The total CPU time for simulating a single 230-s time sequence with Meso-NH, YALES2 and AVBP is given in Table 2. YALES2 and AVBP solvers have an equivalent CPU cost (of about 20,000 CPU hours). Meso-NH solver is twice more expensive: this is mainly due to the structured grid for the Meso-NH case, which is about twice larger than the AVBP/YALES2 unstructured grid.

6 Summary and Conclusions

The present LES multi-model comparison aims at assessing the confidence we can have in the LES of micro-scale meteorology and air pollutant dispersion. For this purpose, a pool of eight different LES models was simulated for the near-neutral MUST trial 2681829 with three different codes: Meso-NH (anelastic formulation, structured grid, IBM), YALES2 (low-Mach formulation, unstructured grid, body-fitted) and AVBP (compressible formulation, unstructured grid, body-fitted). These codes were used with recommended numerical schemes and models, and with highly resolved computational grids (20-30 cm within the array of containers). The dependence of the LES results to user's modelling and numerical choices (i.e. grid resolution and type of elements; advection scheme; subgrid turbulence model) was studied to provide a detailed model-to-model comparison and estimate multi-model variability.

Results were found to remain relatively stable for all codes and all tested configurations. They showed good agreement with the observations available in the MUST dataset, with a low normalized mean square error (NMSE) and a fraction of predictions within a factor of two of observations (FAC2) ranging from 67% in Meso-NH to 76% and 84% in YALES2 and AVBP in the best configurations. This is consistent with previous RANS and LES studies reported in the literature. Results also showed that the multi-model variability is on the order of magnitude of the observation, which is acceptable in air quality problems. This highlights the robustness of the LES approach, which is able to accurately represent high tracer concentration values (the local FAC2 reaches 100% for AVBP and YALES2) and to capture the plume deflection induced by the presence of obstacles.

LES provides detailed information on the early stage of the plume dynamics and is thereby a promising way to dynamically assess, air pollution exposure at the scale of a urban district or an industrial site could be derived. To achieve this purpose, there is also a need to assess the sensitivity of micro-scale LES results to large-scale atmospheric forcing (i.e. mean flow velocity, turbulence intensity and length-scale). Future work includes for instance analysing the influence of the turbulence injection on the vertical plume dynamics and the tracer concentration patterns. This turbulence injection shall be helpful to better represent the cascade of spatial scales involved in air quality problems. It could also be considered as an additional source of uncertainty and variability, so that future work includes estimating the total uncertainties, combining aleatory uncertainties and model structural uncertainties, which are embedded in micro-scale LES.

To further improve the LES models, there is also a need to have access to more informative observations on the near-source dynamics. In this regard, data assimilation can be helpful to design observation networks that are optimised for model development and validation.

References

- [Allwine et al., 2004] Allwine, K., Leach, M., Stockham, L., Shinn, J., Hosker, R., Bowers, J., and Pace, J. (2004). Overview of Joint Urban 2003: An atmospheric dispersion study in Oklahoma City. In *AMS Symposium on planning, nowcasting and forecasting in urban zone*, Seattle, WA.
- [Antonioni et al., 2012] Antonioni, G., Burkhart, S., Burman, J., Dejoan, A., Fusco, A., Gaasbeek, R., Gjesdal, T., Jäppinen, A., Riikonen, K., Morra, P., Parmhed, O., and Santiago, J. (2012). Comparison of CFD and operational dispersion models in an urban-like environment. *Atmos. Environ.*, 47:365–372.
- [Armand et al., 2014] Armand, P., Brocheton, F., Poulet, D., Vendel, F., Dubourg, V., and Yalamas, T. (2014). Probabilistic safety analysis for urgent situations following the accidental release of a pollutant in the atmosphere. *Atmos. Environ.*, 96:1–10.
- [Auguste et al., 2020] Auguste, F., Lac, C., Masson, V., and Cariolle, D. (2020). Large-eddy simulations with an immersed boundary method: Pollutant dispersion over urban terrain. *Atmosphere*, 11(1).
- [Auguste et al., 2019] Auguste, F., Rea, G., Paoli, R., Lac, C., Masson, V., and Cariolle, D. (2019). Implementation of an immersed boundary method in the Meso-NH v5.2 model: Applications to an idealized urban environment. *Geosci. Model Dev.*, 12(6):2607–2633.
- [Aumond et al., 2013] Aumond, P., Masson, V., Lac, C., Gauvreau, B., Dupont, S., and Berengier, M. (2013). Including the drag effects of canopies: Real case large-eddy simulation studies. *Boundary-Layer Meteorol.*, 146(1):65–80.
- [Baklanov, 2000] Baklanov, A. (2000). Application of CFD methods for modelling in air pollution problems: Possibilities and gaps. *Environ. Monit. Assess.*, 65(1):181–189.
- [Bergot et al., 2015] Bergot, T., Escobar, J., and Masson, V. (2015). Effect of small-scale surface heterogeneities and buildings on radiation fog: Large-eddy simulation study at Paris–Charles de Gaulle airport. *Q. J. R. Meteorol. Soc.*, 141(686):285–298.
- [Biltoft, 2001] Biltoft, C. (2001). Customer report for Mock Urban Setting Test. DPG Document No. WDTC-FR-01-121, West Desert Test Center, U.S. Army Dugway Proving Ground, Utah, USA.
- [Blocken and Gualtieri, 2012] Blocken, B. and Gualtieri, C. (2012). Ten iterative steps for model development and evaluation applied to computational fluid dynamics for environmental fluid mechanics. *Environ. Model. Softw.*, 33:1–22.
- [Camelli et al., 2005] Camelli, F., Lohner, R., and Hanna, S. (2005). VLES study of MUST experiment. In *43rd AIAA Aerospace Sciences Meeting and Exhibit*.

REFERENCES

- [Carruthers et al., 1994] Carruthers, D., Holroyd, R., Hunt, J., Weng, W., Robins, A., Apsley, D., Thompson, D., and Smith, F. (1994). UK-ADMS: A new approach to modelling dispersion in the Earth's atmospheric boundary layer. *J. Wind. Eng. Ind. Aerodyn.*, 52:139–153.
- [Challa et al., 2008] Challa, V. S., Indrcanti, J., Baham, J. M., Patrick, C., Rabarison, M. K., Young, J. H., Hughes, R., Swanier, S. J., Hardy, M. G., and Yerramilli, A. (2008). Sensitivity of atmospheric dispersion simulations by HYSPLIT to the meteorological predictions from a meso-scale model. *Environ. Fluid Mech.*, 8(4):367–387.
- [Chang and Hanna, 2004] Chang, J. and Hanna, S. (2004). Air quality model performance evaluation. *Meteorol. Atm. Phys*, 87(1):167–196.
- [Cimorelli et al., 2005] Cimorelli, A. J., Perry, S. G., Venkatram, A., Weil, J. C., Paine, R., Wilson, R. B., Lee, R. F., Peters, W. D., and Brode, R. W. (2005). AERMOD: A dispersion model for industrial source applications. Part I: General model formulation and boundary layer characterization. *J. Appl. Meteorol.*, 44(5):682–693.
- [Clements et al., 2018] Clements, C. B., Lareau, N. P., Kingsmill, D. E., Bowers, C. L., Camacho, C. P., Bagley, R., and Davis, B. (2018). The Rapid Deployments to Wildfires Experiment (RaDFIRE): Observations from the fire zone. *Bull. Amer. Meteorol. Soc.*, 99(12):2539–2559.
- [Colella and Woodward, 1984] Colella, P. and Woodward, P. (1984). The Piecewise Parabolic Method (PPM) for gas-dynamical simulations. *J. Comput. Phys.*, 54(1):174–201.
- [Colin and Rudgyard, 2000] Colin, O. and Rudgyard, M. (2000). Development of high-order Taylor–Galerkin schemes for LES. *J. Comput. Phys.*, 162(2):338–371.
- [Couvreux et al., 2020] Couvreux, F., Bazile, E., Rodier, Q., Maronga, B., Matheou, G., Chinita, M., Edwards, J., van Stratum, B., van Heerwaarden, C., Huang, J., Moene, A., Cheng, A., Fuka, V., Basu, S., Bou-Zeid, E., Canut, G., and Vignon, E. (2020). Intercomparison of Large-Eddy Simulations of the Antarctic Boundary Layer for Very Stable Stratification. *Boundary-Layer Meteorol.*, 176(3):369–400.
- [Crippa et al., 2016] Crippa, M., Janssens-Maenhout, G., Dentener, F., Guizzardi, D., Sindelarova, K., Muntean, M., Van Dingenen, R., and Granier, C. (2016). Forty years of improvements in European air quality: Regional policy-industry interactions with global impacts. *Atmos. Chem. Phys.*, 16(6):3825–3841.
- [Cuxart et al., 2000] Cuxart, J., Bougeault, P., and Redelsperger, J.-L. (2000). A turbulence scheme allowing for mesoscale and large-eddy simulations. *Q. J. R. Meteorol. Soc.*, 126:1–30.
- [de Sampaio et al., 2008] de Sampaio, P., Junior, M., and Lapa, C. (2008). A CFD approach to the atmospheric dispersion of radionuclides in the vicinity of NPPs. *Nucl. Eng. Des.*, 238(1):250–273.

REFERENCES

- [Defforge et al., 2019] Defforge, C. L., Carissimo, B., Bocquet, M., Bresson, R., and Armand, P. (2019). Improving CFD atmospheric simulations at local scale for wind resource assessment using the iterative ensemble Kalman smoother. *J. Wind. Eng. Ind. Aerodyn.*, 189:243–257.
- [Dejoan et al., 2010] Dejoan, A., Santiago, J., Martilli, A., Martin, F., and Pinelli, A. (2010). Comparison between large-eddy simulation and Reynolds-averaged Navier–Stokes computations for the MUST field experiment. Part II: Effects of incident wind angle deviation on the mean flow and plume dispersion. *Boundary-Layer Meteorol.*, 135(1):133–150.
- [Di Sabatino et al., 2007] Di Sabatino, S., Buccolieri, R., Pulvirenti, B., and Britter, R. (2007). Simulations of pollutant dispersion within idealised urban-type geometries with CFD and integral models. *Atmos. Environ.*, 41(37):8316–8329.
- [Donnelly et al., 2009] Donnelly, R., Lyons, T., and Flassak, T. (2009). Evaluation of results of a numerical simulation of dispersion in an idealised urban area for emergency response modelling. *Atmos. Environ.*, 43(29):4416–4423.
- [EEA, 2017] EEA (2017). *Air quality in Europe – 2017 report*. European Environment Agency.
- [Farchi et al., 2016] Farchi, A., Bocquet, M., Roustan, Y., Mathieu, A., and Quérel, A. (2016). Using the Wasserstein distance to compare fields of pollutants: application to the radionuclide atmospheric dispersion of the Fukushima-Daiichi accident. *Tellus B*, 68(1):31682.
- [Fernando et al., 2001] Fernando, H. J. S., Lee, S. M., Anderson, J., Princevac, M., Pardyjak, E., and Grossman-Clarke, S. (2001). Urban Fluid Mechanics: Air Circulation and Contaminant Dispersion in Cities. *Environ. Fluid Mech.*, 1(1):107–164.
- [Filippi et al., 2018] Filippi, J.-B., Bosseur, F., Mari, C., and Lac, C. (2018). Simulation of a large wildfire in a coupled fire-atmosphere model. *Atmosphere*, 9(6).
- [Franke et al., 2011] Franke, J., Hellsten, A., Schlunzen, K. H., and Carissimo, B. (2011). The COST 732 best practice guideline for CFD simulation of flows in the urban environment: A summary. *Int. J. Environ. Pollut.*, 44(1-4):419–427.
- [García-Sánchez and Gorré, 2018] García-Sánchez, C. and Gorré, C. (2018). Uncertainty quantification for microscale CFD simulations based on input from mesoscale codes. *J. Wind. Eng. Ind. Aerodyn.*, 176:87–97.
- [García-Sánchez et al., 2017] García-Sánchez, C., Tendeloo, G. V., and Gorré, C. (2017). Quantifying inflow uncertainties in rans simulations of urban pollutant dispersion. *Atmos. Environ.*, 161:263–273.
- [García-Sánchez et al., 2018] García-Sánchez, C., van Beeck, J., and Gorré, C. (2018). Predictive large eddy simulations for urban flows: Challenges and opportunities. *Build. Environ.*, 139:146–156.

REFERENCES

- [Gourdain et al., 2009] Gourdain, N., Gicquel, L., Montagnac, M., Vermorel, O., Gazaix, M., Staffelbach, G., Garcia, M., Boussuge, J., and Poinso, T. (2009). High performance parallel computing of flows in complex geometries – Part 1: Methods. *Comput. Sci. Discov.*, 2:015003.
- [Gousseau et al., 2011] Gousseau, P., Blocken, B., Stathopoulos, T., and van Heijst, G. (2011). CFD simulation of near-field pollutant dispersion on a high-resolution grid: A case study by LES and RANS for a building group in downtown Montreal. *Atmos. Environ.*, 45(2):428–438.
- [Granet et al., 2010] Granet, V., Vermorel, O., Leonard, T., Gicquel, L., and Poinso, T. (2010). Comparison of nonreflecting outlet boundary conditions for compressible solvers on unstructured grids. *AIAA journal*, 48(10):2348–2364.
- [Grylls et al., 2019] Grylls, T., Cornec, C. M. L., Salizzoni, P., Soulhac, L., Stettler, M. E., and van Reeuwijk, M. (2019). Evaluation of an operational air quality model using large-eddy simulation. *Atmos. Environ.*, 3:100041.
- [Hamburg University, 2002] Hamburg University (2002). *CEDVAL dataset*.
- [Hanna et al., 2002] Hanna, S., Tehranian, S., Carissimo, B., Macdonald, R., and Lohner, R. (2002). Comparisons of model simulations with observations of mean flow and turbulence within simple obstacle arrays. *Atmos. Environ.*, 36(32):5067–5079.
- [Hanna et al., 2004] Hanna, S. R., Hansen, O. R., and Dharmavaram, S. (2004). FLACS CFD air quality model performance evaluation with Kit Fox, MUST, Prairie Grass, and EMU observations. *Atmos. Environ.*, 38(28):4675–4687.
- [Harms et al., 2011] Harms, F., Leidl, B., Schatzmann, M., and Patnaik, G. (2011). Validating LES-based flow and dispersion models. *J. Wind. Eng. Ind. Aerodyn.*, 99(2):289–295.
- [Hayati et al., 2017] Hayati, A. N., Stoll, R., Kim, J. J., Harman, T., Nelson, M. A., Brown, M. J., and Pardyjak, E. R. (2017). Comprehensive Evaluation of Fast-Response, Reynolds-Averaged Navier–Stokes, and Large-Eddy Simulation Methods Against High-Spatial-Resolution Wind-Tunnel Data in Step-Down Street Canyons. *Boundary-Layer Meteorol.*, 164(2):217–247.
- [Hertwig et al., 2019] Hertwig, D., Gough, H. L., Grimmond, S., Barlow, J. F., Kent, C. W., Lin, W. E., Robins, A. G., and Hayden, P. (2019). Wake Characteristics of Tall Buildings in a Realistic Urban Canopy. *Boundary-Layer Meteorol.*, 172(2):239–270.
- [Holmes and Morawska, 2006] Holmes, N. and Morawska, L. (2006). A review of dispersion modelling and its application to the dispersion of particles: An overview of different dispersion models available. *Atmos. Environ.*, 40(30):5902–5928.
- [Klein et al., 2007] Klein, P., Leidl, B., and Schatzmann, M. (2007). Driving physical mechanisms of flow and dispersion in urban canopies. *Int. J. Climatol.*, 27(14):1887–1907.
- [König, 2014] König, M. (2014). Large-eddy simulation modelling for urban scale, Ph.D. thesis. *University of Leipzig*.

REFERENCES

- [Koutsourakis et al., 2012] Koutsourakis, N., Bartzis, J. G., and Markatos, N. C. (2012). Evaluation of Reynolds stress, k - ϵ and RNG k - ϵ turbulence models in street canyon flows using various experimental datasets. *Environ. Fluid Mech.*, 12(4):379–403.
- [Kraushaar, 2011] Kraushaar, M. (2011). *Application of the compressible and low-Mach number approaches to large-eddy simulation of turbulent flows in aero-engines*. Phd thesis, Institut National Polytechnique de Toulouse.
- [Kumar et al., 2015] Kumar, P., Feiz, A.-A., Ngae, P., Singh, S. K., and Issartel, J.-P. (2015). CFD simulation of short-range plume dispersion from a point release in an urban like environment. *Atmos. Environ.*, 122:645–656.
- [Lac et al., 2018] Lac, C., Chaboureau, J.-P., Masson, V., Pinty, J.-P., Tulet, P., Escobar, J., Leriche, M., Barthe, C., Aouizerats, B., Augros, C., Aumond, P., Auguste, F., Bechtold, P., Berthet, S., Bielli, S., Bosseur, F., Caumont, O., Cohard, J.-M., Colin, J., Couvreux, F., Cuxart, J., Delautier, G., Dauhut, T., Ducrocq, V., Filippi, J.-B., Gazen, D., Geoffroy, O., Gheusi, F., Honnert, R., Lafore, J.-P., Lebeaupin Brossier, C., Libois, Q., Lunet, T., Mari, C., Maric, T., Mascart, P., Mogé, M., Molinié, G., Nuissier, O., Pantillon, F., Peyrillé, P., Pergaud, J., Perraud, E., Pianezze, J., Redelsperger, J.-L., Ricard, D., Richard, E., Riette, S., Rodier, Q., Schoetter, R., Seyfried, L., Stein, J., Suhre, K., Taufour, M., Thouron, O., Turner, S., Verrelle, A., Vié, B., Visentin, F., Vionnet, V., and Wautélet, P. (2018). Overview of the Meso-NH model version 5.4 and its applications. *Geosci. Model Dev.*, 11(5):1929–1969.
- [Lafore et al., 1998] Lafore, J. P., Stein, J., Asencio, N., Bougeault, P., Ducrocq, V., Duron, J., Fischer, C., Héreil, P., Mascart, P., Masson, V., Pinty, J. P., Redelsperger, J. L., Richard, E., and de Arellano, J. V.-G. (1998). The Meso-NH atmospheric simulation system. Part I: Adiabatic formulation and control simulations. In *Annales Geophysicae*, volume 16, pages 90–109.
- [Lamberti et al., 2018] Lamberti, G., García-Sánchez, C., Sousa, J., and Gorlé, C. (2018). Optimizing turbulent inflow conditions for large-eddy simulations of the atmospheric boundary layer. *J. Wind. Eng. Ind. Aerodyn.*, 177:32–44.
- [Langmann et al., 2009] Langmann, B., Duncan, B., Textor, C., Trentmann, J., and van der Werf, G. R. (2009). Vegetation fire emissions and their impact on air pollution and climate. *Atmos. Environ.*, 43(1):107–116.
- [Leelőssy et al., 2014] Leelőssy, A., Molnár, F., Izsák, F., Havasi, A., Lagzi, I., and Mészáros, R. (2014). Dispersion modeling of air pollutants in the atmosphere: a review. *Cent. Eur. J. Geosci.*, 6(3):257–278.
- [Liu et al., 1994] Liu, X.-D., Osher, S., and Chan, T. (1994). Weighted essentially non-oscillatory schemes. *J. Comput. Phys.*, 115(1):200–212.
- [Locci et al., 2018] Locci, C., Vervisch, L., Farcy, B., Domingo, P., and Perret, N. (2018). Selective Non-catalytic Reduction (SNCR) of Nitrogen Oxide Emissions: A Perspective from Numerical Modeling. *Flow Turbul Combust*, 100(2):301–340.

REFERENCES

- [Lunet et al., 2017] Lunet, T., Lac, C., Auguste, F., Visentin, F., Masson, V., and Escobar, J. (2017). Combination of WENO and explicit Runge-Kutta methods for wind transport in Meso-NH model. *Mon. Wea. Rev.*, 145(9):3817–3838.
- [Malandain et al., 2013] Malandain, M., Maheu, N., and Moureau, V. (2013). Optimization of the deflated conjugate gradient algorithm for the solving of elliptic equations on massively parallel machines. *J. Comput. Phys.*, 238:32–47.
- [Masson et al., 2013] Masson, V., Le Moigne, P., Martin, E., Faroux, S., Alias, A., Alkama, R., Belamari, S., Barbu, A., Boone, A., Bouysse, F., Brousseau, P., Brun, E., Calvet, J.-C., Carrer, D., Decharme, B., Delire, C., Donier, S., Essaouini, K., Gibelin, A.-L., Giordani, H., Habets, F., Jidane, M., Kerdraon, G., Kourzeneva, E., Lafaysse, M., Lafont, S., Lebeau-pin Brossier, C., Lemonsu, A., Mahfouf, J.-F., Marguinaud, P., Mokhtari, M., Morin, S., Pigeon, G., Salgado, R., Seity, Y., Taillefer, F., Tanguy, G., Tulet, P., Vincendon, B., Vionnet, V., and Voldoire, A. (2013). The SURFEXv7.2 land and ocean surface platform for coupled or offline simulation of Earth surface variables and fluxes. *Geosci. Model Dev.*, 6:929–960.
- [Merlier et al., 2018] Merlier, L., Jacob, J., and Sagaut, P. (2018). Lattice-Boltzmann large-eddy Simulation of pollutant dispersion in street canyons including tree planting effects. *Atmos. Environ.*, 195:89–103.
- [Meroney et al., 1999] Meroney, R. N., Leitl, B. M., Rafailidis, S., and Schatzmann, M. (1999). Wind-tunnel and numerical modeling of flow and dispersion about several building shapes. *J. Wind. Eng. Ind. Aerodyn.*, 81(1):333–345.
- [Meyers, 2008] Meyers, J. (2008). *Quality and Reliability of Large-Eddy Simulations*. ERCOFTAC series ; 12. Springer. First QLES meeting on Quality and Reliability of Large-Eddy Simulation, held October 22–24, 2007 in Leuven (QLES07).
- [Milliez and Carissimo, 2007] Milliez, M. and Carissimo, B. (2007). Numerical simulations of pollutant dispersion in an idealized urban area, for different meteorological conditions. *Boundary-Layer Meteorol.*, 122(2):321–342.
- [Mittal and Iaccarino, 2005] Mittal, R. and Iaccarino, G. (2005). Immersed boundary methods. *Ann. Rev. Fluid Mech.*, 37:239–261.
- [Monin and Obukhov, 1954] Monin, A. and Obukhov, A. (1954). Basic laws of turbulent mixing in the surface layer of the atmosphere. *Contrib. Geophys. Inst. Acad. Sci. USSR*, 24(151):163–187.
- [Mons et al., 2017] Mons, V., Margheri, L., Chassaing, J.-C., and Sagaut, P. (2017). Data assimilation-based reconstruction of urban pollutant release characteristics. *J. Wind. Eng. Ind. Aerodyn.*, 169:232–250.

REFERENCES

- [Moonen et al., 2012] Moonen, P., Dorer, V., and Carmeliet, J. (2012). Effect of flow unsteadiness on the mean wind flow pattern in an idealized urban environment. *J. Wind. Eng. Ind. Aerodyn.*, 104:389–396.
- [Moureau et al., 2011] Moureau, V., Domingo, P., and Vervisch, L. (2011). Design of a massively parallel CFD code for complex geometries. *Comptes Rendus Mécanique*, 339(2-3):141–148.
- [Nicoud and Ducros, 1999] Nicoud, F. and Ducros, F. (1999). Subgrid-scale stress modelling based on the square of the velocity gradient tensor. *Flow Turbul. Combust.*, 62(3):183–200.
- [Paoli et al., 2019] Paoli, R., Poubeau, A., and Cariolle, D. (2019). Large eddy simulations of a reactive solid rocket motor jet. *Submitted to AIAA Journal*.
- [Patnaik et al., 2007] Patnaik, G., Boris, J., Young, T., and Grinstein, F. (2007). Large scale urban contaminant transport simulations with Miles. *J. Fluids Eng.*, 129(12):1524–1532.
- [Perry et al., 2005] Perry, S. G., Cimorelli, A. J., Paine, R. J., Brode, R. W., Weil, J. C., Venkatram, A., Wilson, R. B., Lee, R. F., and Peters, W. D. (2005). AERMOD: A dispersion model for industrial source applications. Part II: Model performance against 17 field study databases. *J. Appl. Meteorol.*, 44(5):694–708.
- [Poinsot and Lele, 1992] Poinsot, T. and Lele, S. (1992). Boundary conditions for direct simulations of compressible viscous flows. *J. Comput. Phys.*, 101(1):104–129.
- [Poubeau et al., 2016] Poubeau, A., Paoli, R., and Cariolle, D. (2016). Evaluation of afterburning chemistry in solid-rocket motor jets using an off-line model. *J. Spacecr. Rockets*, 53(2):380–388.
- [Qian et al., 2018] Qian, Y., Wan, H., Yang, B., Golaz, J.-C., Harrop, B., Hou, Z., Larson, V. E., Leung, L. R., Lin, G., Lin, W., Ma, P.-L., Ma, H.-Y., Rasch, P., Singh, B., Wang, H., Xie, S., and Zhang, K. (2018). Parametric sensitivity and uncertainty quantification in the version 1 of E3SM atmosphere model based on short perturbed parameter ensemble simulations. *J. Geophys. Res.: Atmospheres*, 123(23):13,046–13,073.
- [Ramshaw et al., 1986] Ramshaw, J., O’Rourke, P., and Amsden, A. (1986). Acoustic damping for explicit calculations of fluid flow at low Mach number. Technical report no. LA-10641-MS, Los Alamos National Laboratories, USA.
- [Reymann et al., 2018] Reymann, C., Renzaglia, A., Lamraoui, F., Bronz, M., and Lacroix, S. (2018). Adaptive sampling of cumulus clouds with uavs. *Auton. Robot.*, 42(2):491–512.
- [Sabatier et al., 2020a] Sabatier, T., Largeron, Y., Paci, A., Lac, C., Rodier, Q., Canut, G., and Masson, V. (2020a). Semi-idealized simulations of wintertime flows and pollutant transport in an Alpine valley. Part II: Passive tracer tracking. *Q. J. R. Meteorol. Soc.*, 146(727):827–845.
- [Sabatier et al., 2020b] Sabatier, T., Paci, A., Lac, C., Canut, G., Largeron, Y., and Masson, V. (2020b). Semi-idealized simulations of wintertime flows and pollutant transport in an Alpine valley. Part I: Origins of local circulations. *Q. J. R. Meteorol. Soc.*, 146(727):807–826.

REFERENCES

- [Santiago et al., 2010] Santiago, J. L., Dejoan, A., Martilli, A., Martin, F., and Pinelli, A. (2010). Comparison between large-eddy simulation and Reynolds-averaged Navier-Stokes computations for the MUST field experiment. Part I: Study of the flow for an incident wind directed perpendicularly to the front array of containers. *Boundary-Layer Meteorol.*, 135(1):109–132.
- [Schmitt et al., 2007] Schmitt, P., Poinso, T., Schuermans, B., and Geigle, K.-P. (2007). Large-eddy simulation and experimental study of heat transfer, nitric oxide emissions and combustion instability in a swirled turbulent high-pressure burner. *J. Fluid Mech.*, 570:17–46.
- [Schönfeld and Rudgyard, 1999] Schönfeld, T. and Rudgyard, M. (1999). Steady and unsteady flow simulations using the hybrid flow solver AVBP. *AIAA journal*, 37(11):1378–1385.
- [Smagorinsky, 1963] Smagorinsky, J. (1963). General circulation experiments with the primitive equations: I. The basic experiment. *Mon. Wea. Rev.*, 91(3):99–164.
- [Soulhac et al., 2011] Soulhac, L., Salizzoni, P., Cierco, F.-X., and Perkins, R. (2011). The model SIRANE for atmospheric urban pollutant dispersion. Part I: Presentation of the model. *Atmos. Environ.*, 45(39):7379–7395.
- [Soulhac et al., 2012] Soulhac, L., Salizzoni, P., Mejean, P., Didier, D., and Rios, I. (2012). The model SIRANE for atmospheric urban pollutant dispersion. Part II: Validation of the model on a real case study. *Atmos. Environ.*, 49:320–337.
- [Temel and van Beeck, 2016] Temel, O. and van Beeck, J. (2016). Adaptation of mesoscale turbulence parameterisation schemes as RANS closures for ABL simulations. *J. Turbul.*, 17(10):966–997.
- [Thouron et al., 2020] Thouron, L., Rochoux, M., Jaravel, T., and Vermorel, O. (2020). Large-eddy simulations of the MUST trial 2681829 using AVBP, Meso-NH and YALES2. Technical Report TR-CFD-20-14, CERFACS, Toulouse, France.
- [Tominaga and Stathopoulos, 2013] Tominaga, Y. and Stathopoulos, T. (2013). CFD simulation of near-field pollutant dispersion in the urban environment: A review of current modeling techniques. *Atmos. Environ.*, 79:716–730.
- [Toparlar et al., 2017] Toparlar, Y., Blocken, B., Maiheu, B., and van Heijst, G. (2017). A review on the CFD analysis of urban microclimate. *Renew. Sust. Energ. Rev.*, 80:1613–1640.
- [Vervecken et al., 2015a] Vervecken, L., Camps, J., and Meyers, J. (2015a). Dynamic dose assessment by large eddy simulation of the near-range atmospheric dispersion. *J. Radiol. Prot.*, 35(1):165–178.
- [Vervecken et al., 2015b] Vervecken, L., Camps, J., and Meyers, J. (2015b). Stable reduced-order models for pollutant dispersion in the built environment. *Build. Environ.*, 92:360–367.

REFERENCES

- [Wang and Trouvé, 2004] Wang, Y. and Trouvé, A. (2004). Artificial acoustic stiffness reduction in fully compressible, direct numerical simulation of combustion. *Combust. Theory Model.*, 8(3):633–660.
- [Williamson et al., 2015] Williamson, D., Blaker, A. T., Hampton, C., and Salter, J. (2015). Identifying and removing structural biases in climate models with history matching. *Clim. Dyn.*, 45(5):1299–1324.
- [Working group “GT 3D dispersion”, 2015] Working group “GT 3D dispersion” (2015). *Guide de bonnes pratiques pour la réalisation de modélisations 3D pour des scénarios de dispersion atmosphérique en situation accidentelle*. INERIS, Technical Report, DRA-15-148997-06852A.
- [Yamada and Koike, 2011] Yamada, T. and Koike, K. (2011). Downscaling mesoscale meteorological models for computational wind engineering applications. *J. Wind. Eng. Ind. Aerodyn.*, 99(4):199–216.
- [Yee and Biltoft, 2004] Yee, E. and Biltoft, C. A. (2004). Concentration fluctuation measurements in a plume dispersing through a regular array of obstacles. *Boundary-Layer Meteorol.*, 111(3):363–415.